POLITECNICO DI TORINO

Master degree course in ICT for Smart Societies

Master Degree Thesis

Analysis and design of algorithms for astrometric data reduction

Supervisors
Prof. Bartolomeo Montrucchio
Prof. Monica Visintin
Prof. Deborah Busonero (INAF - OATo)

Candidate
Alessandro Morichetta

Department of Electronics and Telecommunications

Academic Year 2017-2018

Summary

In December 2013 *Gaia* satellite was launched by ESA (European Space Agency). Since the start of the nominal operations in mid 2014 the instrument is collecting all-sky images of our galaxy, the Milky Way.

During its five years of operation the satellite will detect a billion of celestial objects with the goal of calculating with high accuracy, for each of them, the fundamental astrometric parameters: position, proper motion and parallaxes. The accuracy targeted by the mission is in the order of tens microseconds of arc.

The scientific instruments is made of two identical telescopes pointing two fields of view separated by an angle of 106.5° (basic angle) which share a common focal plane. The focal plane is made of 106 CCDs, around 4000 × 2000 pixels each, of which 62 are devoted to astrometry. Each CCD work in TDI (time delayed integration) in synch with the scanning motion of the satellite. The result of the acquisition in the astrometric field (AF) is a collection of small windows sized 12x18 pixels around each observed star.

The data processing is entrusted to DPAC (Data Processing and Analysis Consortium). One of the main systems composing the consortium is the Astrometric Instrument Model (AIM), that is devoted to the calibration of the stellar point spread functions (PSFs) that are subsequently used to evaluate the astrometric parameters. AIM is one of the software systems run in data processing center in Turin (DPCT) with the supervision of the staff of Istituto Nazionale di AstroFisica (INAF), and in particular Osservatorio Astrofisico di Torino (OATo).

In order to create a template of the stellar profiles to use in the astrometric parameter computation, oversampling is performed by overlapping multiple images belonging to "similar" exposures. In particular, stellar observations are considered on a daily basis and then grouped into classes . Each variable that is related to the shape of the stellar profiles (ex. CCD position, stellar

magnitude and spectrum) introduces a further subdivision of the observations into classes. This procedure allows to merge (overlap) only images that share the same characteristics and, in a subsequent step, to use curve fitting to obtain customized PSF templates for each class of observations.

One of the variables that are considered in the calibration phase is the *AC (across-scan) motion*, which is the shift of the stars on the focal plane in the perpendicular direction to the scanning direction. This motion is caused by the precession of the spin axis of the satellite, that allows to have a uniform sky coverage during acquisition. The resulting effect is a periodical vertical deformation, or smearing, of the stellar images. AC motion is empirically computed and the value is quantized into seven levels, which correspond to a further set of possible configurations of the observations.

The work of the thesis is focused in characterizing the speed of the star in the focal plane, both in across-scan (AC) and in along-scan (AL) direction, in order to attempt a compensation of the smearing effect by shrinking the observation windows. This process would allow to reduce the complexity of the calibration phase, by eliminating one variable from the system and cutting down the number of classes in which the whole dataset is subdivided. In addition, deleting AC (and AL) motion from the stellar profile would allow, together with a proper image up-sampling procedure, to build PSF templates directly on the individual images, avoiding in this way to introduce spurious information by merging different observations. Finally, investigation on periodical variations on images can be performed by removing the main component, which is linked to the satellite precession.

The whole work is implemented in Python. The project includes image processing techniques to shrink the stellar profiles and the computation of image descriptors to verify the effectiveness of the AC motion compensation. Such indicators are computed on the basis of the histogram and the co-occurrence matrix of the image, which describe respectively both the group and pixel-by-pixel properties of the acquired windows. Then, time-domain and frequency-domain analyses are performed to investigate on the presence of periodical components within the collections.

Three experiments were conducted implementing different approaches to shrink the stellar profiles. In particular, one of them foreseen the application of the scanning law model to quantify the exact motion of the stars within the focal plane during the integration period. The aim was to create a procedure that would have act as independently as possible on the AC motion error allowing to separate the effect from other variables impacting on the acquired images. The rationale applied in the thesis project was to introduce as little errors and artefacts as possible, in order to match with the high precision required by the *Gaia* mission.

Even though most of the applied techniques allowed to mitigate the deformation of the PSFs, it was not possible to completely eliminate the periodic effect. Moreover, the analysis of descriptors allowed to observe that, also when the shrinking algorithm succeeded in reshaping the stellar profiles, the morphological properties of the pixels remained affected by the perturbation of the AC motion.

A further development of the implemented techniques could manage to compensate the motion effect and to allow an independent PSF calibration on the singular stellar images, that could be then compared to the traditional processing routine.

Contents

List of Tables

List of Figures

Chapter 1

Introduction

1.1 Astrometry

Astrometry is defined as the astronomical discipline concerned with the accurate measurement of the positions and motions of celestial objects, including stars within or outside our Galaxy, planets and other solar system bodies [1].

1.1.1 Angles, distances and motions

Astrometry is essentially concerned with the measurement of ***angles***.

At a first approximation, neglecting the knowledge of the distance of a star or any other celestial object, it is possible to determine its position as it appears projected on the celestial sphere. Such reference system is simply an extension of the one used for geographical positioning, where the definitions of latitude and longitude are revisited to determine the two angular coordinates on the celestial sphere. The commonly used reference unit is the degree. A circle consists in three hundred and sixty degrees, a degree is subdivided into sixty minutes of arc, and each minute of arc is divided into sixty seconds of arc.

Due to the small aperture of the pupil, the human eye can distinguish details up to one minute of arc. Then, the invention of the telescope and the improved accuracy of the instruments during the centuries, allowed observations with a precision of one second of arc. The turbulent motion of the atmosphere imposes a limit on the achievable accuracy, but the latest technologies, such as interferometers and adaptive optics allowed to overwhelm this limit: it is now possible to obtain on-ground observations with accuracies of about tens of microseconds of arc (μas), but only in very narrow fields.

Only space astronomy, in the late 20th century, allowed to perform surveys of the entire sky with accuracy under the milliseconds of arc (*mas*).

Michael Perryman [1] proposes few practical examples to quantify these angles, : the Sun and the Moon both cover an angle of about half a degree on the sky. One second of arc, instead, corresponds to the size of a Euro coin viewed from a distance of 5 km. HIPPARCOS space mission reached accuracies of one *mas*, that corresponds to the diameter of a human hair seen from 10km. *Gaia* satellite is expected to reach accuracies of a few μas, corresponding to a Bohr radius viewed from a distance of 1m.

Apparently, stars seem to be fixed with respect to each other, and the only motion the human eye can perceive is the spinning of the Earth around its axis with a period of twenty four hours that causes a collective movement of the stars.

Actually, every star is moving independently through space. Since the first report of Edmond Halley in 1718, the astronomers started measuring what it is called ***"proper motion"***, i.e. the angular position of each star changes with time due to its motion through space, and not due to other effects like Earth's rotation.

The star motion on the celestial sphere can then be characterized as a sum of multiple components: the slight angular motion due to its velocity through space, plus a tiny apparent oscillatory motion due to the Earth's annual motion around the Sun. Other higher-order components include the effects of binary companions, the influence of planets orbiting around them, and general relativistic effects, that have to be considered and properly studied by modern astronomers in order to achieve the highest accuracies.

It is important to underline that without knowing the star's distance, it is not possible to measure its actual speed through space, but only its angular shift on the celestial sphere. Computing stars distances is therefore needed to convert their angular motion into a true space velocity, but also to convert other observed properties, such as the apparent brightness, into true physical quantities, such as the intrinsic luminosity. Those essential ingredients allow to study the composition, the internal structure and the evolution of the celestial objects in time.

The revolution of the Earth around the Sun during the time period of one year allows to view the space and its objects under slightly different perspectives: the minuscule back-and-forth motion of the stars can then be used to measure their distances from Earth. The star's ***parallax angle*** corresponds to the ratio of the Earth-Sun distance to that of the star: nearby stars, such as Proxima Centauri, have big oscillations, in the order of one second of arc, with respect to the distant stars.

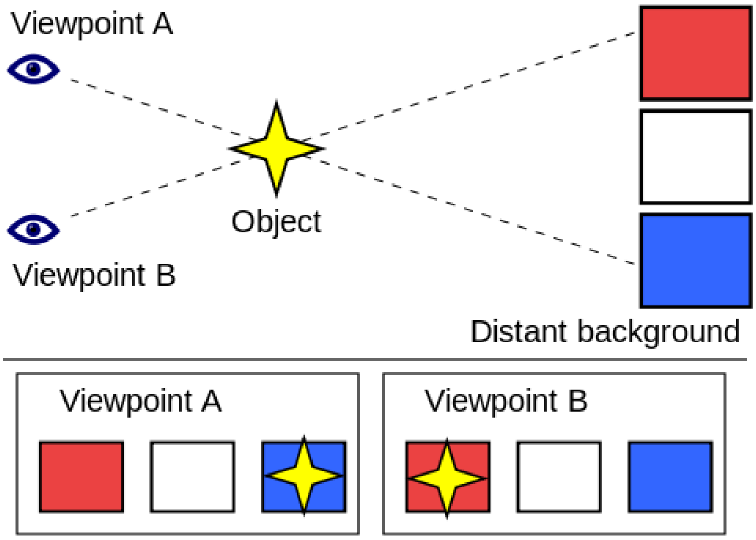

Figure 1.1: Graphical explanation of the parallax concept.

Since the first measurement in 1830s, the technique based on parallax was so used that the fundamental unit of distance in astronomy is based upon it: the *parsec* ("parallax" + "second of arc") describes the distance at which a star has a parallax angle of one second of arc as the Earth moves in its yearly revolution around the Sun [1].

1.1.2 Applications

The measurement of precise distances is not itself the ultimate objective of astronomers. As previously mentioned, what is of primary interest is not only the construction of an astronomical reference frame, but mainly the possible contribution of the astrometric measures towards the knowledge of the properties of the celestial objects, and in a larger scale, the knowledge of the structure, origin and age of our Galaxy up to the whole Universe.

For example, improvements in accuracy led to revolutionary scientific advances, such as the understanding of the motion of the Earth and the consequent acceptance of the heliocentric model. The first successful measurement of stellar parallax is credited to Friedrich Bessel which, in 1838, quantified for the first time the vastness of the Universe. Exact observations allow also to keep UTC atomic time synchronized to Earth's rotation. Astrometric measurements do also contribute in extra-solar planet detection and in determining the distribution of dark matter in the galaxy.

1.1.3 History

Since thousands years ago, when the early humankind started looking up at the sky, *astrometry* and *astronomy* have been basically synonyms until few decades ago, when other types of astronomical investigation became possible.

Determining positions of stars and constellation has been of primary importance for the humankind since ancient times for practical reasons, such as navigation and agriculture, but had also strong implications in the religious sphere, as the celestial objects and events were seen as divine manifestations.

The introduction of the telescope and the advances in instrumentation have steadily improved angular accuracies. Especially, technical advances resulted in telescope improvements, control of measurement errors, and in a growing ability in graduating and further subdividing angular sections on the celestial sphere.

Despite the advances in the instrumentation , obtaining accurate measurements from the ground remained extremely challenging until the last century due to the insurmountable problems imposed Earth's atmosphere. Until the mid 1990s, for instance, ground-based parallaxes were available only for just 8000 stars [2].

As astrometric measurements and the related scientific advances reached a steady point, many other astronomical disciplines rapidly advanced in scientific interest, such as spectroscopy and cosmology, especially when observations opened up in other electromagnetic frequency domains, such as in the radio, infrared, and X-ray.

Only the coming of space astrometry gave a new life to this discipline: the HIPPARCOS satellite of the European Space Agency (ESA) measured in the early 1990s the absolute parallax of 117955 objects with *mas* accuracy, revealing the structure and the evolution of stars and the dynamics of stars, stellar groups, and in a vaster scale, the Milky Way [2].

Figure 1.2 shows how the technological development through centuries improved the astrometric accuracies, in the estimation of star positions and parallaxes.

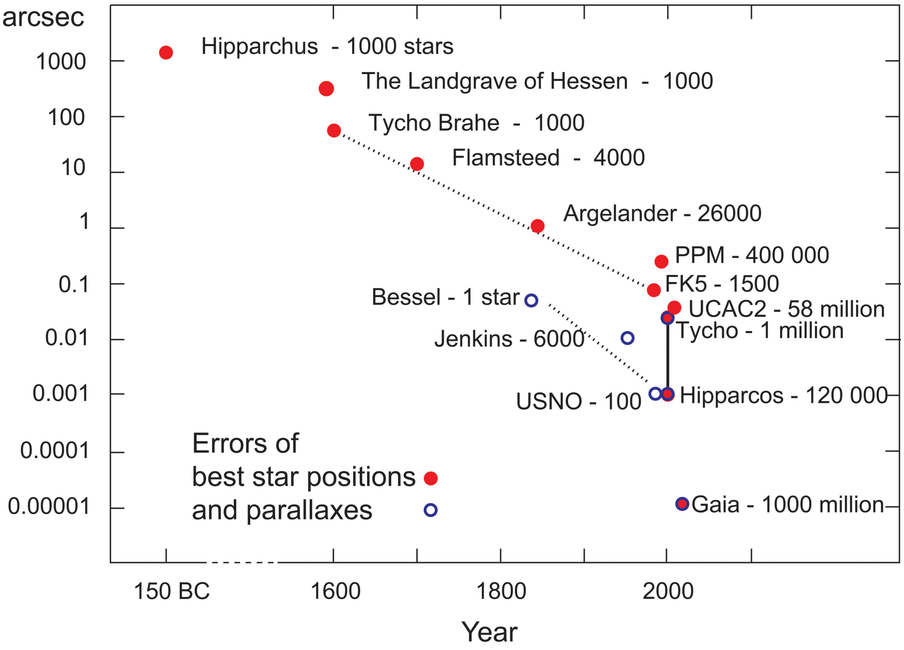

Figure 1.2: Evolution of the astrometric accuracy, both in estimating position and parallaxes. Credit: ESA.

1.2 The Gaia mission

All the algorithms and analyses implemented for the scope of this work exploit the data coming from the Gaia satellite.

Gaia is the astrometric mission developed by ESA (European Space Agency) aimed at producing an all-sky catalog of the Milky Way, determining positions, proper motions and parallaxes. Launched on 19 December 2013, was proposed in the early 1990s by Perryman and Lindegren as an interferometric concept (originally GAIA was spelled as Global Astrometric Interferometer for Astrophysics), but then a direct-imaging approach was preferred. The five-years nominal operations phase started in mid 2014, after a period of commissioning and verification [2].

Gaia determines astrometric data for about one billion objects in the Galaxy, that represent about 1% of the stars in the Milky Way, covering a magnitude range from 6 to 20. It is expected to reach accuracies in the range of 8-25 microseconds of arc [6]. Those measurements allow to determine astrophysical properties, such as surface gravity and temperature, and to understand the origin, the structure, and the evolution of our Galaxy [2].

The instrument, the data acquisition and processing of the Gaia satellite will be discussed in Section 2.

1.3 Thesis overview

The thesis was developed with the collaboration and under the supervision of Osservatorio Astronomico di Torino (OATo), that is part of Istituto Nazionale di AstroFisica (INAF). The institute is one of the main parties of the Data Processing and Analysis Consortium (DPAC) devoted to the data analysis of the *Gaia* satellite.

The work is focused on the development of an alternative approach in the data calibration phase. In particular the attention is focused on the study of the periodical effect that the precession of the satellite produces on the stellar images, introducing a blurred response.

The idea is to study the relation between causes and effects in order to act on the acquired images and operate through the proper image processing techniques in order to reduce or totally eliminate the deformation of the star profiles.

This operation would, at first, exactly quantify the smearing effect of the satellite precession on the images, but also, through the total compensation of the effect itself, allow the identification of other possible periodical variations that can be related to an anomalous instrument response or to other external factors.

1.3.1 Structure of the thesis

Section 2 briefly introduces the *Gaia* mission, describing the astrometric instrumentation devoted to data acquisition (Sect. 2.2) and, then, the operational routine implemented for data processing (Sect. 2.3).

Section 3 will then describe the environment and the data used for the scope of the thesis. The image processing and image analysis tools implemented are therefore reported, together with the mathematical model built to describe the image blurring effect and to relate it to the satellite motion .

Section 4 offers a description of the procedure and the associated experiments that make use of the tools presented in the previous chapter, comparing the results obtained.

Further considerations and a discussion about possible future developments are taken into account in Sect. 5.

Chapter 2

Context

2.1 The spacecraft

The *Gaia* spacecraft, built by the Aerospace Industry Airbus under European Space Agency (ESA) commitment, is equipped with two identical three mirror anastigmatic telescopes, with apertures of 1.45 m x 0.50 m.

The angular resolution of the telescope is approximately given by $\frac{\lambda}{D}$ where λ is the wavelength of the light source and D is the telescope aperture.

The two viewing directions are separated by the *basic angle* $\gamma = 106.5°$. The two associated fields of view, referred as FOV1 and FOV2, indicate respectively the preceding and the following telescope scanning the sky (Fig. 2.1).

The two telescopes share a common focal plane, merging the two beams into a common path at the exit pupil and then folded twice to accommodate the 35 m focal length.

As some asymmetric optical aberrations are present in the optics, the measured star positions is affected by slight chromatic shifts of the diffraction images. For this reason, part of the on-ground data processing foresees uses the color information provided by the photometric detectors in the satellite [2] (Sect. 2.2).

The Gaia spacecraft orbits around the second Lagrange (L2) point of the Sun-Earth-Moon system. This point is located 1.5 million km from Earth and co-rotates with the Earth in its one-year orbit around the Sun. The satellite moves in a Lissajous orbit with an orbital period of nearly 180 days.

Some of the benefits of a Lissajous orbit around L2 point are, for instance, stable thermal conditions, a low impact of radiations, and being the Sun, Earth, and Moon outside the fields of view of the instrument, a high observing

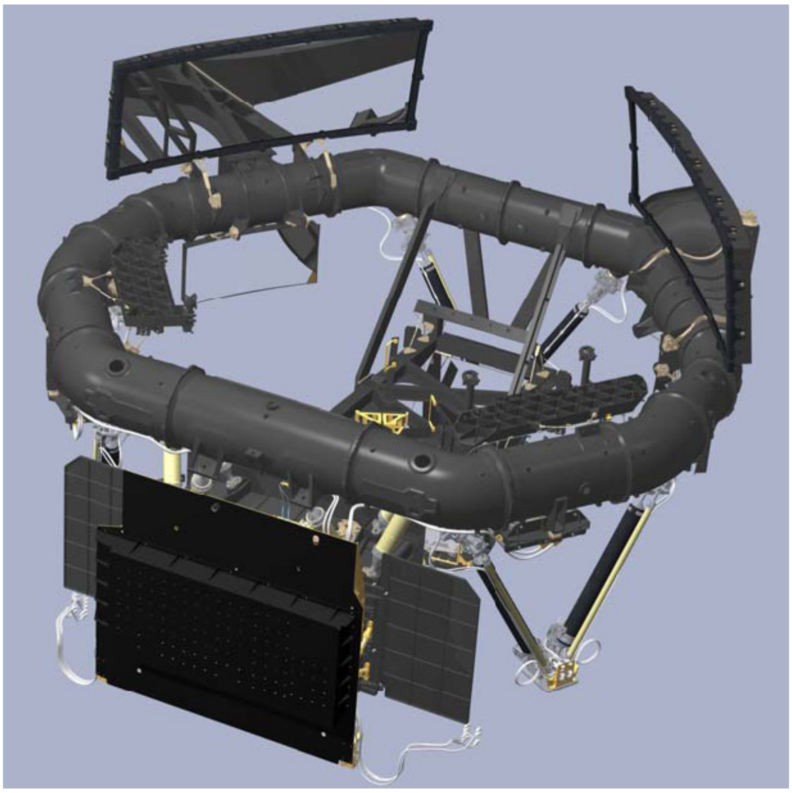

Figure 2.1: Payload of the *Gaia* spacecraft. Credits: Airbus DS.

efficiency. Moreover, by design, the orbit of *Gaia* is not affected by eclipses of the Sun by the Earth during its five-year nominal lifetime [2].

A further description of the *Gaia* Nominal Scanning Law (NSL) will be given in Sect. 3.

2.2 The instruments

As previously mentioned, the focal plane is common to both telescopes, and carries 106 CCD (charge-coupled device) detectors (Fig. 2.2). Not all the CCDs have the same function, and five groups of detectors can then be identified:

- The two wave-front sensing (WFS) and the two basic angle monitoring (BAM) devices, are devoted to metrology. In particular WFS monitor the optical quality of the telescopes, while BAM detectors measure variations in the basic angle between the two telescopes;

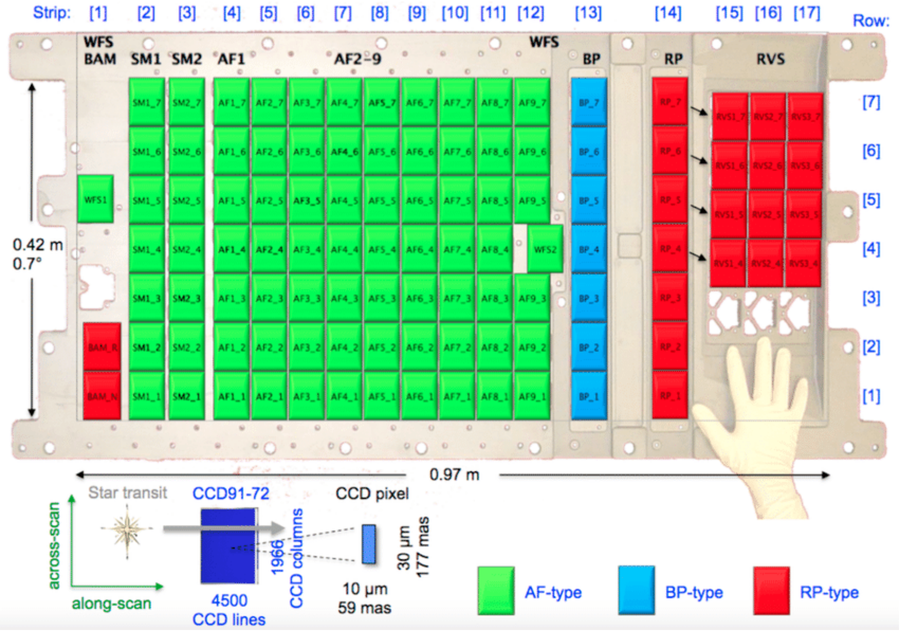

Figure 2.2: Schematic representation of the focal plane assembly. Credits: Airbus DS and Boostec Industries.

- The two sky mappers (SM1 and SM2) CCD strips are devoted to object detection and to the rejection of cosmic rays, Solar protons, or other unwanted elements. Each telescope has its own of sky mappers strip, each one formed by 7 CDDSs;
- The astrometric field (AF) houses 62 CCDs and is devoted to astrometric measurements;
- The 14 blue and red photometers (BP and RP) are used for low-resolution spectro-photometry. Spectra are generated through the use of a blue and a red prism;
- The radial-velocity spectrometer (RVS) 12 CCDs are devoted to spectroscopy.

The motion of the stars on the focal plane identifies the along-scan (AL) direction, while the across-scan (AC) direction is orthogonal to the AL. The 106 CCDs are then arranged on 7 AC rows and 17 AL strips, forming a 938-million-pixels detector.

Each CCD is a back-illuminated, full-frame device with an image area of 4500 lines in the along-scan direction and 1966 columns across-scan. Each pixel has size of 10 μm x 30 μm (corresponding to 58.9 mas x 176.8 mas on the sky), and a full-well capacity of around 190000e-.

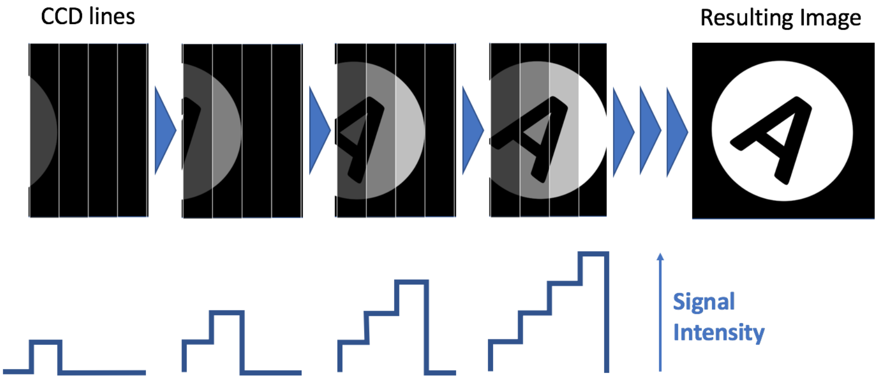

Figure 2.3: Schematic representation of TDI concept.

Since the spacecraft is continuously spinning around its axis with rate $\omega_z = 60$ arcsec/s, each CCD has to be operated in time-delayed integration (TDI), that allows to collect charges as the object images move over the detector. The line shift period of TDI is of 982.8 μs matches the sidereal velocity on the focal plane (scanning velocity) with the CCD transfer velocity (the clock rate) [3]. The integration time per CCD is then of about 4.42 seconds, corresponding to the 4500 TDI lines along-scan multiplied by the fundamental shift period.

In order to avoid pixel saturation for bright objects, a set of 12 electrodes (TDI gates) are connected at distinct positions along the 4500 TDI lines. These TDI-gate electrodes allow to temporarily (or permanently) inhibit the charge transfer over the integration lines, such that the TDI integration time is effectively reduced to the remaining number of lines between the gate and the readout register. The 4500-lines integration is then used only for faint objects. Available integration times are 4500, 2900, 2048, 1024, 512, 256, 128, 64, 32, 16, 8, 4, and 2 TDI lines, and can be chosen based on configurable look-up tables depending on the brightness of the object, the CCD, the field of view, and the across-scan pixel coordinate [2].

The photo-electron count, after read-out, is converted into ADU (analog-to-digital units) by a 16-bit analog-to-digital converter (ADC).

The amount of data produced by the 106 CCDs operated in time-delayed integration with a line shift period of about 1 ms would be too big to be directly transmitted to the ground. Thus, an on-board data reduction procedure is needed:

1. Readout on astrometric field (AF) CCDs is limited to only small windows around objects of interest; The along-scan window size in AF is 18 pixels for stars that are brighter than 16 mag and 12 for fainter objects. In very dense areas, only the brighter stars are observed. The across-scan dimension of the window is 12 pixels;
2. The two-dimensional images (windows) are, except for stars brighter than 13 mag, binned in the across-scan direction, returning a one-dimensional signal but preserving the scientific information content (timing/along-scan centroid, total intensity/magnitude, and spectral information);
3. The resulting intensity profiles, such as line-spread functions or spectra, are compressed on board without loss of information;

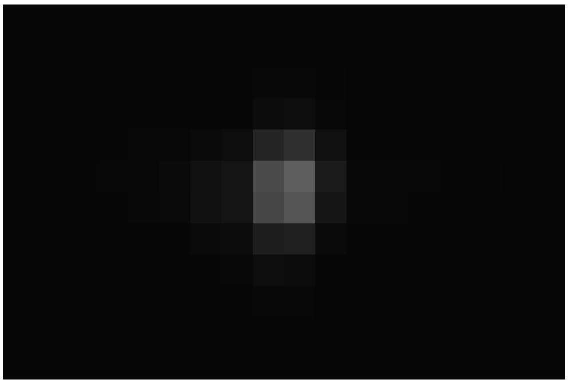

Figure 2.4: Example of 12x18 pixel window acquired by the *Gaia* instrument.

The astrometric devices allow to detect wavelength in the range of 330-1050 nm and, unlike its predecessor HIPPARCOS, *Gaia* does not select its targets within a predefined input catalogue loaded on board, but performs an unbiased survey of the sky.

2.3 The data processing

Once acquired, the *Gaia* measurements need to be processed, which means that the CCD data have to be calibrated and transformed into astrophysical quantities.

It is possible to identify two classes of data processing: daily and cyclic. The daily systems process the *Gaia* telemetry in near-real time as it comes

Astrometric Instrument Parameters	Value
Basic Angle	$\gamma = 106.5°$
Focal length	$F = 35$ m
Telescope aperture	$D_x = 0.5$ m, $D_y = 1.4$ m
Scan rate	$\omega_z = 60$ arcsec/s
TDI integration time (without gating)	4416.7032 s
Pixel size ALxAC	10 x 30 μm (58.9 x 176.8 mas)

Table 2.1: List of the main astrometric parameters of Gaia instrument.

down from the spacecraft, while the cyclic processing iterates between calibration and the determination of source parameters by repeatedly processing all the *Gaia* data until the system converges.

The processing of the data coming from the *Gaia* spacecraft is committed to the Data Processing and Analysis Consortium (DPAC), a pan-European collaboration of several hundred astronomers and software specialists [2]. The Consortium is organized into Coordination Units (CUs), each one in charge of different tasks. CU3, in particular, takes care of what is called *core processing*, that consists in reconstructing with high accuracy the astrometric parameters of a subset of well-behaved stars (single stars, photometrically and astrometrically stable, not too faint, etc), and to transform such information into positional and physical parameters. [4]

Since this procedure is critical and requires a complex data analysis, independent procedures/models are designed and implemented with the aim of comparing the results with baseline processing. The verification system that operates independently from the baseline data reduction chain is the *Astrometric Verification Unit (AVU)*. AVU comprises three systems: *the Basic Angle Monitoring (BAM)*, the *Global Sphere Reconstruction (GSR)* and the ***Astrometric Instrument Model (AIM)***. The main duty of the AIM software system is to monitor and calibrate the Gaia astrometric response.

AIM is basically an object oriented software model written in Java language and operated in ALTEC (Torino), where the Astrometric Verification Unit has its own Data Processing Center (DPCT) [4].

Gaia collaboration does not have data rights. After processing, calibration, and validation inside DPAC, catalogues are made available to the world without limitations. Several intermediate releases, with roughly a yearly cadence, have been defined.

The latest *Gaia* data release version was 1.1 version the second data release

(DR2), published on 9th July 2018 [8].

2.3.1 The Astrometric Parameters Estimation

Gaia data processing is divided in daily tasks and a global cyclic processing.

The initial step of the data processing consists in obtaining a first estimation of the star positions and flux, together with an initial evaluation of the attitude, which describes the instantaneous orientation of the spacecraft with respect to the reference frame. This procedure is known as Initial Data Treatment (IDT), and is performed on a daily basis.

This initial process includes also the calibration of CCD bias, sky background, and the calculation of preliminary colours, which are required to select the adequate PSF (or LSF) model for the final image fitting. The detailed calibration of the image parameters is still not part of the pre-processing.

The final step of IDT consists cross-matching the on-board detections with a catalogue of astronomical sources, after a proper filtering spurious detections. One catalogue source is assigned to each detection, and a new source is added if no one is found.

Then, the iterative *astrometric core solution* software system is in charge of determining the astrometric parameters, like parallax and proper motion. The astrometric core solution also refines the instrument calibration and attitude estimation made in the previous data processing steps.

Finer calibrations lead to a better estimation of image parameters, which again lead to improve the astrometric and photometric solutions, leading to better calibrations, etc. The cross-matching and source list generation processes are also repeated during these cycles, in order to have a more precise distinction between spurious and genuine detections [7].

Tasks	Daily	Cyclic
Raw data reconstruction	Final	
Basic angle variations determination	Final	
On-ground attitude reconstruction	Preliminary	
Bias and astrophysical background	Preliminary	Final
Astrometric PSF/LSF calibration	Preliminary	Final
Spectro-photo image parameter determination	Preliminary	
Astrometric image parameter determination	Preliminary	Final
Cross-match processing	Preliminary	Final

Table 2.2: Pre-processing steps, divided in daily and cyclic systems.

The cyclic processing allows to mitigate the systematic effects produced by the instrument during time scales in the order of days or entire revolutions, which is required to reach the target accuracies.

For example, selecting a wrong PSF model could introduce errors up to *mas* resolution which can not be mitigated or eliminated by any calibration procedure at a later time.

2.3.2 The PSF/LSF calibration

The AIM processing strategy is based on 24 hours of observed data for stars with magnitude brighter than 16 mag [3].

Many different software modules are involved in the daily processing. In particular, the *Raw Data Processing (RDP)* module is in charge of estimating the image parameters of observations with magnitude brighter than 16. The *Daily Calibration* module, instead, is in charge of reconstructing the stellar profiles on daily basis. Since the beginning of the scientific operations, AIM has run an algorithm devoted to the reconstruction of the point spread functions (PSFs) or, in case of binned windows, line spread functions (LSFs), which are basically the instrument responses acquired by the CCDs.

The calibration procedure has to take into account all the causes that may affect significantly the PSF/LSF profiles, such as the dependence on the source color (the spectral distribution of the star), and the change of the instrument response within the focal plane.

The idea is to find a mathematical model of the signal profile, that could be representative of the different regions of the focal plane and of stars belonging to a wide range of magnitude and spectral type. In order to achieve this goal, the fit optimization must be statistical, that means based on a collection of signals and not the individual exposure [5]. In addition, combining a large set of elementary observations allows to increase the signal to noise (S/N) ratio and obtain an oversampled instrument response. The residual errors of the elementary exposed are also supposed to be averaged and removed by the oversampling procedure.

For this reason, at each run, the observations collected during a 24-hours period are gathered into different groups identified by the unambiguous combination of CCD involved in the detection, field of view (FOV1 or FOV2), spectral type and magnitude of the stars. More precisely, the spectral type and the magnitude do not indicate a precise frequency or mag values, but define bins with certain tolerance intervals [3].

Dividing the observations into classes allow to build PSF or LSF templates that are as much error-free as possible, avoiding to merge signals that belong to different configurations. It is also assumed that the CCD response do not vary during the daily interval. Before proceeding with the calibration, outliers are also discarded from the collection in order to avoid to include in the analysis also observations affected by anomalies, such as exceeding peculiarities in their spatial structure, spectral distribution, temporal variability, astrometric behavior, and so on [5].

As many variables are considered to discriminate the observations, the greater will be the number of possible configurations resulting in a finer division of the exposure into classes. Having more classes, as mentioned, increase the precision of the PSF templates as the amount of error derived by the overlapping of images belonging to different stars is reduced. However, a finer class separation results in a reduced numerosity within each class, and it may not satisfy the oversampling specifications. The dataset could be enriched by enlarging the time period in which exposure are collected, preferring for example a monthly cyclic process to the daily routine presented here, but it would introduce a new variable, the time, during which the instrument response may change with non-negligible effects.

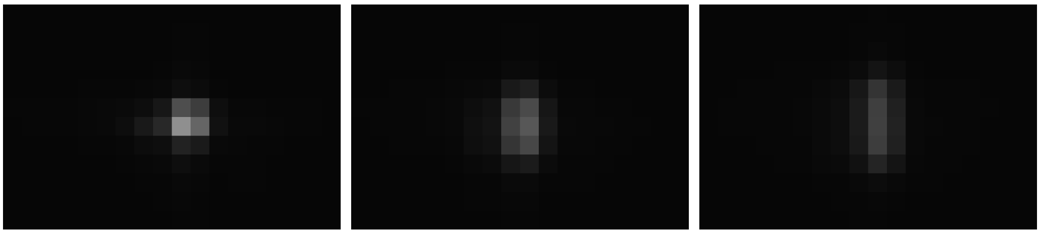

(a) `AC_motion = 0` (b) `AC_motion = 3` (c) `AC_motion = 6`

Figure 2.5: Comparison of three *Gaia* images with different levels of `AC_motion`.

The precession of the satellite introduces a vertical component in the speed of the stellar image (i.e. a speed in AC direction), causing a periodical smearing effect, with period of 3 hours. This element can be considered as an added variation from nominal behavior of the observations. For this reason, AIM software also experimentally evaluates the rate of the stellar images in the across-scan direction by computing the AC shift of the image within the row of 9 CCDs over which the star transits, and dividing this quantity by the transit time. The evaluation of this quantity introduces a further division within the datasets: six levels of *AC motion* are identified, and the observation belonging to each level have to be treated independently for the PSF/LSF reconstruction.

Fig. 2.5 reports three examples of stellar images belonging to different AC motion levels. When the motion is minimum, a compact and highly exposed profile is obtained. When the motion is consistent, the stellar profile appears stretched and underexposed due to the fact that the star has moved across the focal plane during the integration period.

Once this step is performed, overlapping of stellar profiles is performed using proper registration algorithms. The resulting oversampled PSF/LSF profile will no more have the original pixel coordinates, but will have a new wider set of real coordinates referred to the centroid of the registered exposures. An example of these high resolution profiles is given in Fig. 2.6.

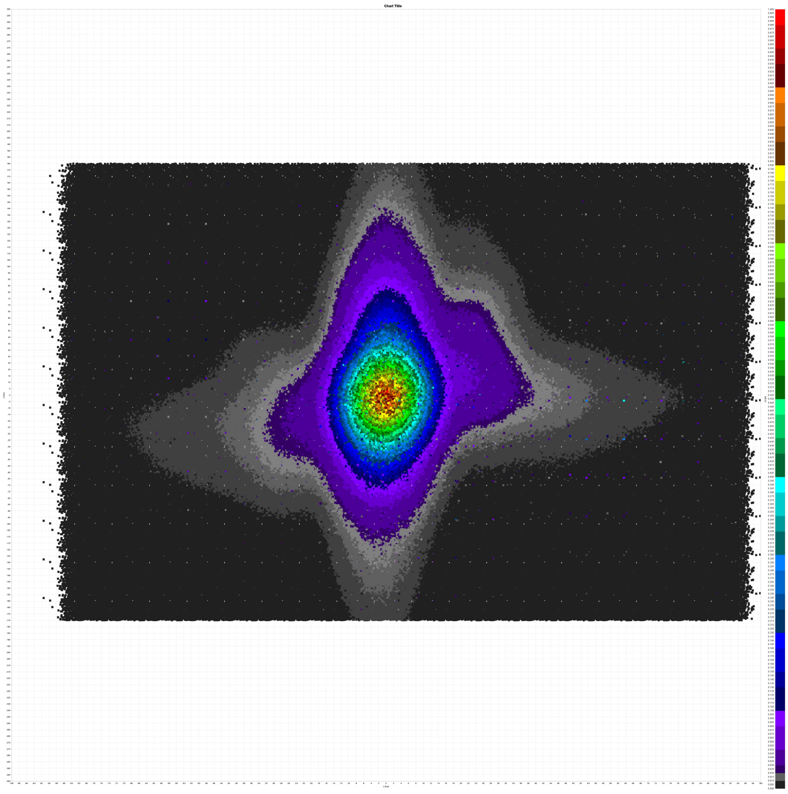

Figure 2.6: Example of oversampled PSF profile, obtained by overlapping thousands of exposures. The observations belong to the preceding field of view (FOV1) and were acquired by CCD with coordinates (4,5) in the focal plane. The star spectral type bin is 641nm, while the magnitude bin is 9. Courtesy of OATo.

The approach used by AIM for the fit foresees to expand the PSF profiles into a sum of orthogonal and spatially invariant functions, and adjusting properly the coefficients in order to describe the instrument response variation over the field of view and for the specific magnitude and spectral type of the stars [5].

At a first approximation, let us consider an LSF produced by a binned window. The detected signal can be described by a function $f = (x_k - \tau_T)$, where x_k with $k = 1, ..., K$are the pixel positions and τ_T is the "true" photocenter position. As previously mentioned, the actual signal would not be an elementary exposure, but a high-resolution representation of the instrument response obtained combining a large set of observations.

The fitting process will produce, following a maximum likelihood approach, an output function $\tilde{f}(x_k)$, that will be an approximation of the input function f. While the usual approach would be in minimizing the discrepancy $h(x_k)$:

$$h(x_k) = f(x_k - \tau_T) - \tilde{f}(x_k) \tag{2.1}$$

the actual goal is to minimize the astrometric error on position δ_T when the fit result $\tilde{f}(x_k)$ is used as a template within the location algorithm on new collections of exposures.

The LSF is modeled using a set of monochromatic basis functions derived from a $sinc^2$ parent function, that represents in an ideal (aberration-free) case the signal generated by a light with wavelength λ passing through a telescope of with focal length F, with a rectangular slit having width L_ξ:

$$\psi_0^m(x) = (sinc\rho)^2 = \left[\frac{\sin\rho}{\rho}\right]^2, \rho = \pi\frac{xL_\xi}{\lambda F} \tag{2.2}$$

with x being the focal plane coordinate.

Higher-order functions are built starting from the parent function and its derivatives:

$$\psi_n^m(x) = \left(\frac{d}{dx}\right)^n \psi_0^m(x) \tag{2.3}$$

Then, the polychromatic functions are obtained by weighting the monochromatic functions by their spectrum discretized components S_l [5]:

$$\psi_n(x) = \sum_l S_l \psi_n^m(x; l) \tag{2.4}$$

The approach that is used for PSF fitting is basically an approximation performed combining the along-scan and across-scan LSF models (Fig. 2.7). However, this methodology is known to limit the performance, as PSFs are typically asymmetric, and therefore can not be optimally fitted by this representation. Hence, new 2-D PSF models are being built starting from two-dimensional basic functions to be used in future [8].

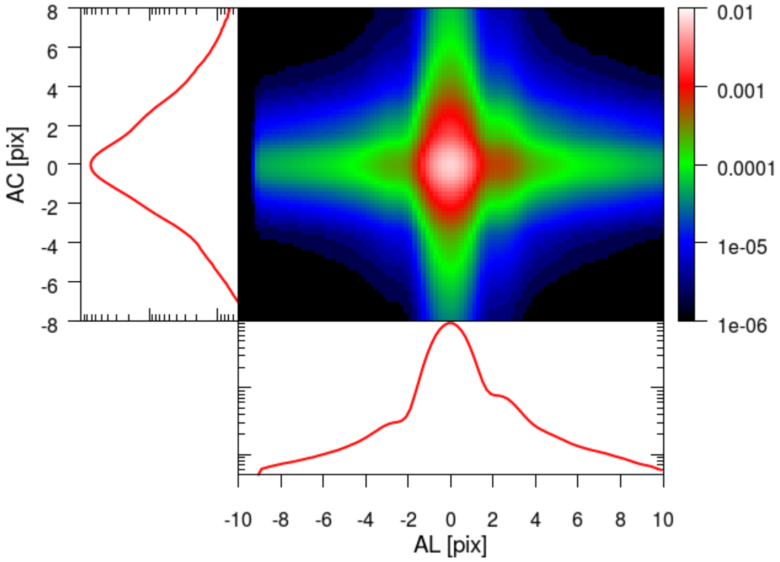

Figure 2.7: Example of PSF profile obtained by cross product of the AC and AL LSF models [8].

2.4 Motivation of the thesis

As anticipated during the Introduction, the thesis project is aimed at proposing an alternative approach for the calibration of the stellar profiles.

The traditional routine foresees to build the PSF templates by fitting oversampled profiles that are obtained by the registration of multiple observations. This methodology allows to treat the stellar profiles on a daily-basis satisfying the precision required by the mission specification.

Despite allowing to increase the S/N ratio, overlapping images belonging to different stars and captured under different configurations may introduce in the calibration procedure a certain amount of error that could be not negligible. In addition, the process of image registration can in turn introduce errors.

For this reason, a methodology based on computing the PSF templates directly on the individual images is proposed.

In particular, the work is focused on the attempt of compensating the distorting effect of the satellite precession, mainly evident in the across-scan motion. The shrinking of the stellar profiles is performed using image processing techniques, and the results are evaluated through the use of indicators based on the study of the image histogram and of the image co-occurrence matrix.

Deleting the AC (and AL) motion from the astrometric images allows to remove one of the variables that are involved in the traditional calibration process, reducing the dimension and the complexity of the problem. In addition, stellar profiles cleaned from the smearing effect of satellite precession can be used to retrieve the PSF model for each singular image, avoiding to introduce errors due to the registration of different observations.

The analysis of the image descriptors as a function of time allows to study periodical variations of the image properties, which may be linked to some hidden fenomena related to the astrometric instrument or to external factors.

Chapter 3

Data and tools

3.1 The Environment

3.1.1 Python language

The whole work of this study is implemented in Python. Python is an object oriented language that proposes a simple syntax, with dynamic typing and a high readability. Despite computing performance not being the strong point of Python, the huge amount of libraries available and the characterizing modularity of this language contribute in easing the development of complex applications.

In particular, several Python packages are exploited for the purpose of this study in order to implement image and time sequence processing, methods for data reduction and representation.

3.1.2 Python libraries

The main Python libraries used in the implementation of the thesis project is listed below:

- `NumPy`: Python package that allows to manage multi-dimensional data and to perform scientific calculations upon that. In the specific case of this work NumPy is used to perform basic operations on 1-D and 2-D data, polynomial approximation of digital sequences, and linear transformations on images;
- `SciPy`: an other fundamental scientific toolbox for performing mathematical operations in the Python environment. In particular, it is used to interpolate one-dimensional sequences and to perform FFT;

- `OpenCV`: is a software library - originally developed in C++, now available in C, Python and Java language - aimed at providing tools for Computer Vision. Concerning this work, the `cv2` Python library is used to re-scale images using specific interpolation algorithms and to compute image moments when needed.

3.2 The Data

3.2.1 Gaia wrappers

In order to perform the analysis on real data, several datasets are provided by the OATo.

These datasets are organized into ***wrappers***, that gather all the information about a certain set of observations (or transits) and are stored in a specific `.gbin` format.

Generally, it is possible to retrieve a wrapper containing the information collected under a precise configuration: for example, in this application, wrappers collect data belonging to a specific class of stars (identified by their magnitude and spectrum bins) and a specific Field Of View (FOV), acquired by a specific CCD, during a specific time interval.

Usually wrapper data are gathered during a period of 24 hours but, depending on the cardinality of the specific class of star, this time interval can be enlarged. This methodology comes with the need to retrieve a data collection that is as much stable and functional as possible for the desired analysis: if we want to characterize a set of observations, we need that no significant variations and anomalies occur during the acquisition period. In addition, as to take advantage of the most dense collections as possible, only wrappers belonging to class of stars with wavelength bin 641.4 nm are considered in this work.

In particular, for the scope of this project, `CalWrappers` are used: a specific implementation of Gaia wrappers that contain the complete data relative to the astrometric calibration.

Each `CalWrapper` contains information about the overall collection: such as the CCD coordinates (CCD row, CCD strip), the timestamps of the first and the last transits characterizing the collection, the field of view which the collections belongs to and the variables characterizing the class of stars. In addition, each wrapper stores the raw data that describe each single observation, such as the timestamp of the acquisition, the raw samples (in ADU) of the relative window, the estimation of the biases and error sources, and calibration parameters.

All the used variables will be listed and discussed in more detail in Section 3.2.3.

3.2.2 The Python data structure

In order to easily access all the information, an object oriented data structure is built using Python classes.

In particular, the `Observation` and `Wrapper` classes are implemented to store, respectively, the data related to the single transits and the properties of the entire set. In addition to representing the collection attributes, the two classes implement the basic methods to access and operate on the dataset.

3.2.3 Variables definition

In this section the variables relevant for this study will be listed and briefly described.

Table 3.1 lists the attributes of the Wrapper that are common to the entire collection. Table 3.2 refers to the attributes of the single observations.

Wrapper.class attributes		
Attribute name	Type	Meaning
`id`	string	ID of the wrapper
`first_obs`	int	OBMT timestamp of the first observation of the collection (ns)
`last_obs`	int	OBMT timestamp of the last observation of the collection (ns)
`time_interval`	float	Time interval between the first and last observation (hours)
`n_transits`	int	Total number of observations in the collection
`ccdRow`	int	AC (across-scan) coordinate of the CCD in the focal plane
`ccdStrip`	int	AL (along-scan) coordinate of the CCD in the focal plane
`mag`	int	Magnitude bin of the class of stars in the collection (mag)
`wavn`	int	Wavelength bin of the class of stars in the collection (nm)
`fov`	boolean	`fov`=0 for FOV1, `fov`=1 for FOV2
`observations`	list<`Observation`>	Collection of the `Observation` objects

Table 3.1: List of attributes of the Wrapper class implemented in Python.

As indicated in the description of the `Wrapper` parameters, the wavelength and magnitude attributes of the stars composing the collection do not refer to precise values, but indicate a bin of values.

The `AC_rate` parameter of the Observation class is not the actual computation of the instantaneous image speed on the across-scan direction, but an empirical evaluation of this quantity, obtained by computing the vertical

Observation.class attributes		
Attribute name	Type	Meaning
`id`	string	Index of the observation within the collection
`integration_time`	float	Exposition time (ms) depending on the gating used
`timestamp`	int	Timestamp (ns) from J2000.0 date
`AC_rate`	float	Empirical evaluation of the AC rate by AIM
`window`	list<list<float»	Raw samples of the 12x18 pixels window (16-bit ADU)

Table 3.2: List of attributes of the Observation class implemented in Python.

shift of the image during the transit on the entire CCD row and dividing by the transit time.

3.3 Image processing tools

Most of the methods implemented for the scope of this work deal with image processing. In particular, the experiments carried out during this project require to locate the star profiles, defining regions of interest (ROIs) around the light blobs of the stars. Then, this portion of image is used to extract information about the profile shape and other morphological features through the call of appropriate functions.

Nevertheless, the execution of these tasks require an image rescaling, as the small size of the observation windows (12x18 pixels) do not allow any kind of analysis.

3.3.1 Image Interpolation

As anticipated, image scaling is performed as a preliminary operation in order to have a more detailed definition of the ROI and to allow a further analysis on stellar profiles. The operation, performed through interpolation, certainly generates spurious information, but sophisticated methodologies can help in reducing the amount of error introduced.

For this purpose, the `resize` method of the `OpenCV` Python library is exploited. As mentioned, of great importance in this operation is the choice of the proper interpolation algorithm. The `OpenCV` library offers five interpolation methods:

- `INTER_NEAREST`: performs a nearest-neighbor interpolation
- `INTER_LINEAR`: a bilinear interpolation

- `INTER_AREA`: resampling using pixel area relation
- `INTER_CUBIC`: a bicubic interpolation over 4x4 pixel neighborhood
- `INTER_LANCZOS4`: a Lanczos interpolation over 8x8 pixel neighborhood

In order to choose the best performing algorithm, all the possible configurations were compared (see Fig. 3.1), and the Lanczos interpolation has been preferred.

(a) `INTER_NEAREST` (b) `INTER_LINEAR` (c) `INTER_AREA`

(d) `INTER_CUBIC` (e) `INTER_LANCZOS4`

Figure 3.1: Comparison of `OpenCV` interpolation algorithms. Lanczos interpolation 3.1e seems to return a smoother image.

3.3.2 ROI detection

Many Python libraries, such as `scikit-image` and `openCV` provide methods to locate blobs within images but an ad-hoc method was preferred, in order to have much more control in a large set of images, and in case, improve the location methods directly.

The implemented method consists in defining a region of interest (ROI) by scanning the image rows one by one and finding the column indexes that define the full width at half maximum (FWHM) interval.

FWHM is widely used in physics, statistics and signal processing to define, for example, the dispersion of a distribution or the bandwidth of a signal. In this case FWHM is used to delineate the star profile within the image.

The maximum 16-bit ADU value is determined within the whole image, and it is used to define the intervals within each row that has ADU values greater than the half of the maximum value. The algorithms also foresees the possibility to raise or lower the threshold in order to obtain a wider or tighter region.

Once the operation is complete, a rectangle is defined such as all the intervals relative to each row are inscribed.

Still, the algorithm has to scan element by element all the pixels of the image, requesting a complexity proportional to the area of the image. As this action is performed after the interpolation, the computational time of this operation could be not negligible.

Once this rectangular area is defined, the function devoted to this algorithm allows to set a flag in order to decide to consider or not for the subsequent analysis the pixels of the ROI that were falling out of the FWHM intervals.

3.3.3 ROI analysis

It is possible to perform some analysis to characterize the images and evaluate the deformation of the star profile due to the image speed on the focal plane during the integration period. For each image two different types of features are computed: the first, that deals with the moments of the intensity histogram of the image; the second, obtained with the evaluation of the image co-occurrence matrix [9].

Histogram moments The histogram of an image is a graphical tool for representing the occurrence of the intensity levels within the image. More precisely, the image histogram $p(z_i)$ computes the number of pixels that have the intensity z_i, with z being a random variable denoting the intensity, with $i = 0,1,2,...,L-1$being the distinct intensity levels. In our case, 16-bit images produce $L = 2^{16} = 65536$ intensity levels. The statistical n-th central moment of the histogram is defined as

$$\mu_n = \sum_{i=0}^{L-1} (z_i - m)^n p(z_i) \tag{3.1}$$

where m is the mean value of z, i.e. the average intensity within the image:

$$m = \sum_{i=0}^{L-1} z_i p(z_i) \tag{3.2}$$

Eq. (3.1) can be used to determine the following image descriptors:

- *Variance (second moment)* $\sigma^2(z) = \mu_2(z)$: it is used to measure the contrast of an image that can be consequently a descriptor of smoothness (the lower the contrast, the smoother the image).

- *R (normalized variance)*: since variance tends to take very large values especially for 16-bit grayscale images, the normalized quantity R is computed using the following expression:

$$R = 1 - \frac{1}{1 + \sigma^2(z)} \tag{3.3}$$

- *Third moment* $\mu_3(z)$: is used as a measure of the degree of symmetry of the histogram. It assumes negative values for images skewed to the left and positive values for images skewed to the right, so it can be used to assess if the image is underexposed or overexposed.

- *Uniformity* $U(z)$: as described by the definition in Eq. (3.4), it reaches a maximum for images in which all intensity levels are equal (maximally uniform).

$$U = \sum_{i=0}^{L-1} p^2(z_i) \tag{3.4}$$

- *Average entropy* $e(z)$: this descriptor expresses the inverse concept of uniformity: the higher the entropy, the higher the variability. It is computed as:

$$e(z) = -\sum_{i=0}^{L-1} p(z_i) \log_2 p(z_i) \tag{3.5}$$

The above mentioned quantities allow to gather information for describing the texture of an image as a whole, but do not consider the relative position of the pixels. Therefore, it is necessary to consider other descriptors that take into account this aspect. In order to do this, a co-occurrence matrix of the image is computed.

Co-occurrence matrix Given an image f with L possible intensity levels, and given an operator Q that defines the relative position of a pair of pixels within the image, the *co-occurrence matrix* (also known as *GLCM* Gray-Level Co-occurrence Matrix) of image f can be defined as the matrix G whose element g_{ij} indicates the number of times in which a couple of pixels in the position specified by Q take respectively intensities $z_i$and z_j, where

$1 \leq i, j \leq L$.. Matrix G will then have dimensions $L \times L$. An example of co-occurrence matrix is shown in Fig. 3.2.

Of course, a large number L of intensity levels imply very large co-occurrence matrices, so it is common use to create bins of intensities in order to reduce the dimension of the G matrix. For the purpose of this analysis, the intensities of the stellar images were quantized into $K = 256$ levels instead of the $L = 65536$ levels of the 16-bit ADUs.

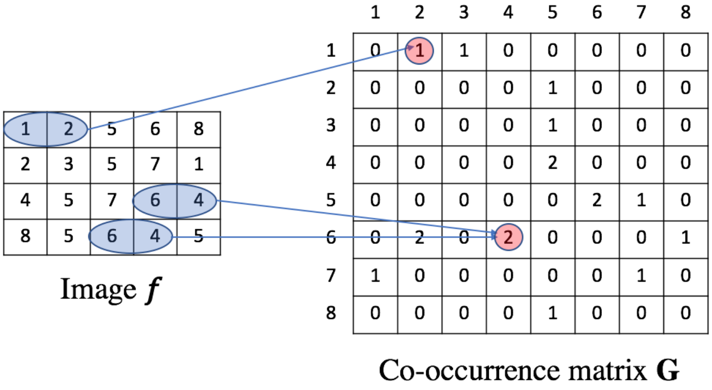

1	2	5	6	8
2	3	5	7	1
4	5	7	6	4
8	5	6	4	5

	1	2	3	4	5	6	7	8
1	0	1	1	0	0	0	0	0
2	0	0	0	0	1	0	0	0
3	0	0	0	0	1	0	0	0
4	0	0	0	0	2	0	0	0
5	0	0	0	0	0	2	1	0
6	0	2	0	2	0	0	0	1
7	1	0	0	0	0	0	1	0
8	0	0	0	0	1	0	0	0

Figure 3.2: On the left, a sample 3-bit image f as a function of the 8 intensity levels z, on the right, the corresponding co-occurrence matrix G, built defining the operator Q in such a way that each couple of pixels considered is formed by "one point immediately on the right with respect to the other".

Of great importance in this analysis is the definition of the operator Q: in our case defined the relative position between two pixels as "one immediately on the right with respect to the other". The probability that a pair of points will have values (z_i, z_j) is then defined by

$$p_{ij} = g_{ij}/n \tag{3.6}$$

where n is the number of pixel pairs that satisfy the operator Q. Being:

$$m_r = \sum_{i=1}^{K} i \sum_{j=1}^{K} p_{ij} \tag{3.7}$$

$$m_c = \sum_{j=1}^{K} j \sum_{i=1}^{K} p_{ij} \tag{3.8}$$

$$\sigma_r^2 = \sum_{i=1}^{K}(i - m_r)^2 \sum_{j=1}^{K} p_{ij} \tag{3.9}$$

$$\sigma_c^2 = \sum_{j=1}^{K}(j - m_c)^2 \sum_{i=1}^{K} p_{ij} \tag{3.10}$$

we can define the following descriptors:

- *Correlation*: measures for each couple of points how much a pixel is correlated to its neighbor. It can take values from -1 to 1 corresponding to perfect negative and perfect positive correlations.

  $$\sum_{i=1}^{K}\sum_{j=1}^{K} \frac{(i - m_r)(j - m_c)p_{ij}}{\sigma_r \sigma_c} \tag{3.11}$$

  with $\sigma_r \neq 0$ and $\sigma_c \neq 0$.

- *Contrast*: a measure of the intensity contrast between the couple of pixels. Its values run from 0 to $(K - 1)^2$.

  $$\sum_{i=1}^{K}\sum_{j=1}^{K}(i - j)^2 p_{ij} \tag{3.12}$$

- *Energy* (or *uniformity*): measures the uniformity of the image in the range [0,1]. Uniformity is equal to 1 for a constant image.

  $$\sum_{i=1}^{K}\sum_{j=1}^{K} p_{ij}^2 \tag{3.13}$$

- *Homogeneity*: measures the closeness of the co-occurrence matrix G to a diagonal matrix. It takes values in the range [0,1], being 1 for G diagonal.

  $$\sum_{i=1}^{K}\sum_{j=1}^{K} \frac{p_{ij}}{1 + |i - j|} \tag{3.14}$$

In the implementation of this analysis, the `graycomatrix` and `graycoprops` methods of the `scikit-image` Python library were used to respectively retrieve the co-occurrence matrix G and extract its features. The library allowed to compute two more descriptors:

- *Dissimilarity*: similar concept of the contrast descriptor, but the weights increase linearly (0,1,2,3, ...) as one moves away from the diagonal, instead of quadratically (0,1,4,9, ...).

$$\sum_{i=1}^{K}\sum_{j=1}^{K} |i-j| p_{ij} \tag{3.15}$$

- $\sqrt{ASM}$: it coincides with the square root of the Energy feature, that is named Angular Second Moment within the `scikit-image` environment.

The construction of the co-occurrence matrix G foresees to pass as argument to the `graycomatrix` the distance and the angles that define the direction of the operator Q. A further documentation about the descriptors evaluated by the `graycoprops` method can be found in the Mryka Hall-Beyer tutorial [10].

3.4 Analysis of periodicity

It is possible to evaluate how the image descriptors vary as function of time if the analysis of the stellar profiles is performed image by image within a collection of exposures, . Periodical variations within the data set are therefore detected, if present.

An important application of this analysis is the modeling of the periodical deformation caused by the speed component of the image during the transit on the focal plane. This effect has a precise periodicity of 3 hours, which is a consequence of the precession rate of the satellite, whereas the amplitude of those oscillations depend on the position on the focal plane (Fig. 3.3).

Since the work of this thesis is aimed at compensating the effects of such oscillations, a periodical analysis on the image properties is also performed to verify the effectiveness of the correction, and therefore to investigate on the presence of other possible periodical variations.

The analysis in the frequency domain is performed computing the FFT of the 24-hours evolution of each descriptor (Fig. 3.3b). The plots show the periods in abscissa instead of the frequencies in order to have an immediate understanding of the main periodical components.

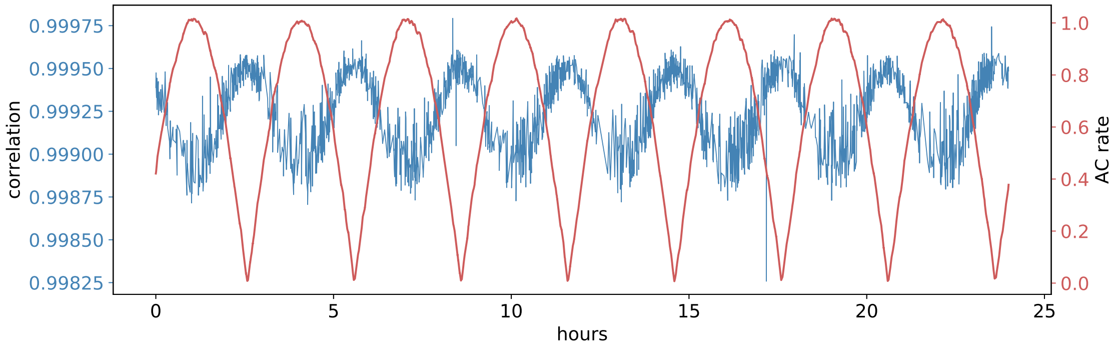

(a)

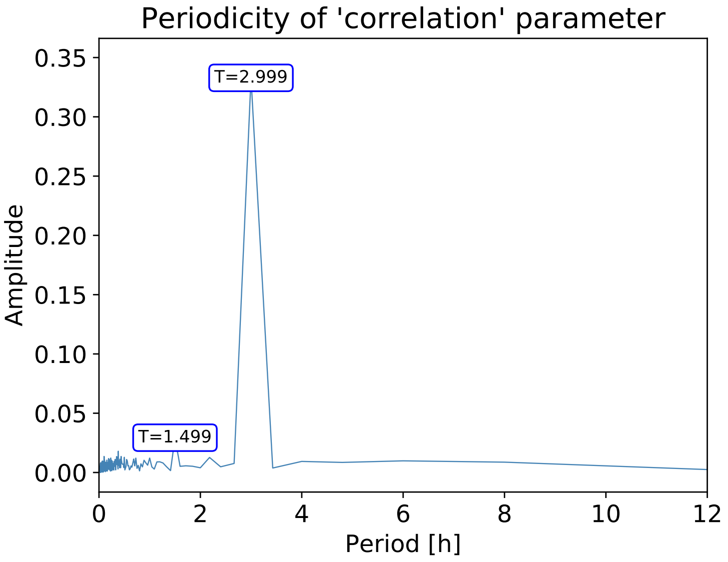

(b)

Figure 3.3: (a) Example of periodicity analysis in the time domain. The picture represents in blue the values of the *'correlation'* descriptor evaluated for the thousands of transits of the collection. The feature, evaluated in the 24-hours period, is compared to the evolution of the AC rate empirically evaluated by the AIM software. (b) Analysis in the frequency domain.

3.5 Image smearing model

A fundamental step in the processing of the star profiles is the modeling of the smearing effect in both along (AL) and across (AC) direction due to the precession of the satellite. The knowledge of a mathematical model of the motion of the satellite as a function of time allows to measure the instantaneous speed of the stellar image among the focal plane, and consequently allows to quantify the deformation of the star profile during the integration period. In this way, it is possible to separate the effect of the precession from other possible error sources that may introduce deformation on the PSF profiles.

In order to achieve this goal, the Nominal Scanning Law of the satellite (NSL) is studied and the evolution of AL and AC rates within the time interval of interest is computed. Once these quantities are retrieved, it will be possible, for each observation, to evaluate the smearing of the stellar image by integrating the quantities during the exposition period.

3.5.1 Nominal Scanning Law (NSL)

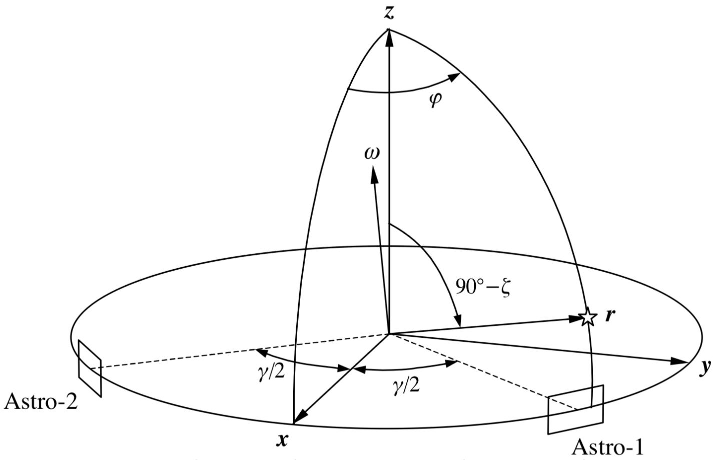

Figure 3.4: Scanning Reference System of the Gaia satellite: z is the spin axis of the satellite and x is chosen as the bisector of the two viewing directions; ϕ and ζ are the spherical coordinates that indicate the direction of the star with respect to the reference system; γ=106,5° is the basic angle dividing Astro-1 and Astro-2 that are, respectively, the preceding and following field of views. [11]

The Nominal Scanning Law is the model describing the instantaneous pointing (attitude) of the *Gaia* instrument as function of time. The main motion that governs the satellite is the rotation around its spin axis with a period of 6 hours. In addition, the spin axis itself is very slowly precessing (63-days-period) around the solar direction at a fixed solar-aspect angle of 45 degrees. Over 5 years of nominal operations, *Gaia* will complete 29 precession periods, allowing a uniform coverage of the sky.

Once defined the Scanning Reference System [x y z] as in Fig. 3.4, the position of a star can be defined by its spherical coordinates (ϕ, ζ). The along-scan (AL) field angle is η, defined by the relation:

$$\eta = \phi - \psi \tag{3.16}$$

where $\psi = \pm\gamma/2$ is the location of the field center in case of, respectively, preceding or following field of view (FOV1 or FOV2), with γ being the basic angle.

The speed of the source on the focal plane will be determined then by the two components in the along (AL) and across (AC) directions, respectively $\eta'(= \phi')$ and ζ'. Given the NSL, according to Lindegren (2004) [11] the two quantities will vary sinusoidally according set of equations:

$$\eta' = -\omega_z + |z'| \cos(\Omega + \phi) \tan\zeta \tag{3.17}$$

$$\zeta' = -|z'| \sin(\Omega + \phi) \tag{3.18}$$

where z' is the precession rate and Ω is the spin phase, which defines the angle between the plane containing the Sun and the instrument z axis and the instrument zx plane.

In order to derive the quantities needed for the computation of AL and AC rate, the Fortran routine provided by SOFA (Standards Of Fundamental Astronomy Board of the International Astronomical Union) is exploited. The algorithm takes as input a reference time interval and a sampling frequency, and returns as output the sampled values of the parameters that describe the Those quantities are: time instant (days from J2000.0), sun ecliptic longitude (deg), sun velocity (rad/sec), Ω (rad), $d\Omega/dt$ (rad/sec). Once those values are retrieved it is possible to compute the evolution with time of the η' and ζ' parameters.

3.5.2 Example

Figure 3.5 shows η' and ζ' functions evaluated in a 24-hours period with a ‘dt’ of 1 second. If the values are needed for a real case scenario, it is necessary to use as input the timestamps of the observations, properly translated into Julian Dates, and to set the initial parameters of Ω_0 and ν_0.

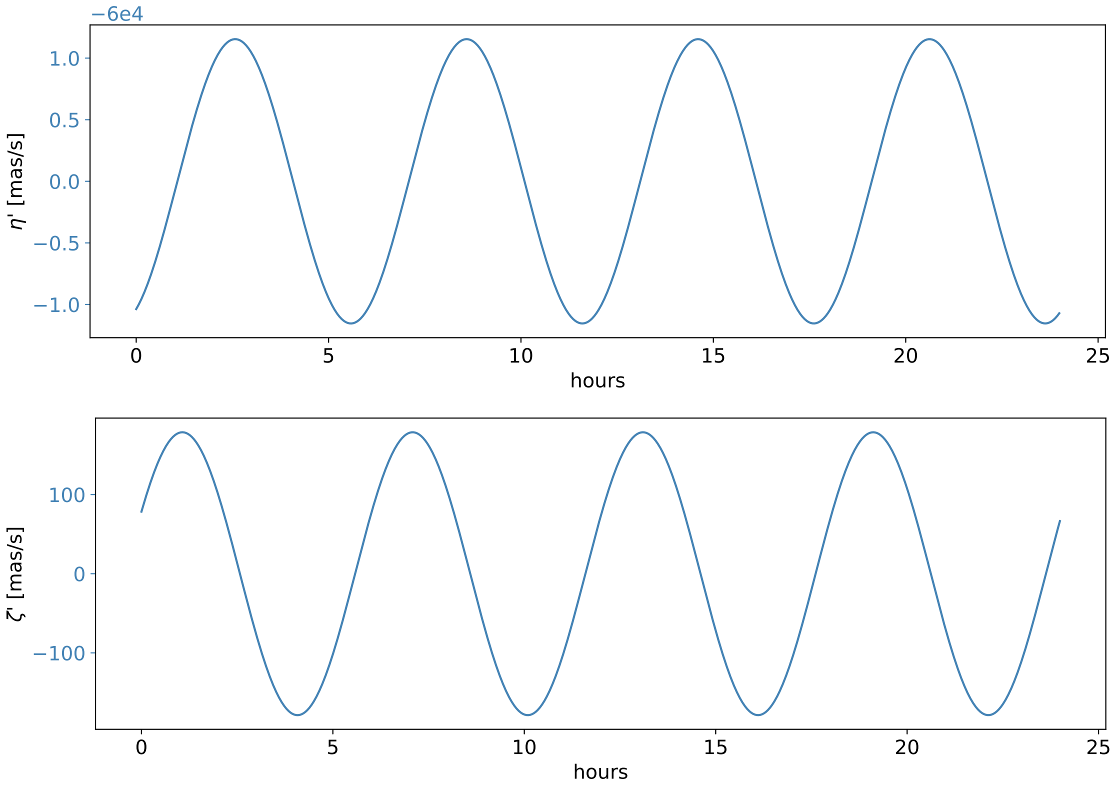

Figure 3.5: The picture on top and the one at the bottom describe, respectively, the trend of η' and ζ' during an interval of 24 hours.

The two functions both show an evident periodicity of 6 hours. AC rate is known to have an amplitude, in absolute value, of up to 174 mas/s, while AL rate has a much smaller deviation from $-\omega_z$: for a central transit it vanishes, but at extreme edges $\zeta = 0.36°$ it may have an amplitude of about 1.1 mas/s [11]. Once those quantities are determined for each time instant, it is possible to apply it to quantify the effect of AC smearing.

Known the size of a pixel, that is $10\mu m$ (58.9 mas) in the AL direction and $30\mu m$ (176.8 mas) in the AC direction, and supposing a constant scan rate within the integration period, it is possible to have a first approximation on how much the image is smeared by the star speed on the field of view.

The relations that allow to have an estimate of AC and AL smearing (in pixels, or a fraction of pixel) are the following (see Fig. 3.6):

$$AL\_smearing = I * (|\eta'(t_0)| + \omega_z)/px_{AL} \tag{3.19}$$

$$AC\_smearing = I * |\zeta'(t_0)|/px_{AC} \tag{3.20}$$

Where I is the integration period for the specific observation, while px_{AL} and px_{AC} are respectively the pixel sizes in along and across direction (in mas). t_0 indicates the instant in which η' and ζ' are sampled The w_z offset in the `AL_smearing` formula was added as a component of the speed in the AL direction is synchronous to the spinning of the satellite around its z axes.

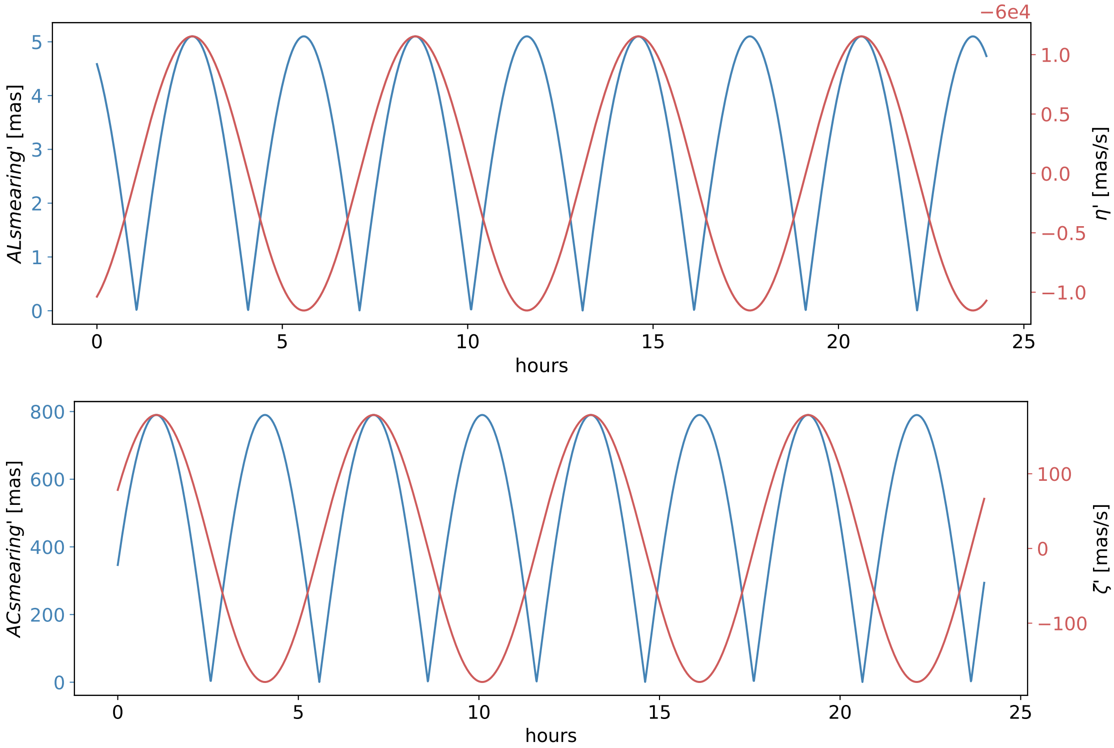

Figure 3.6: Effect of the spacecraft's precession, in terms of deformation (in pixels) of the star profiles. The smearing in along and across directions is reported in blue. The red lines recall the AL and AC speed of the star on the focal plane as function of time.

The analysis took into consideration the "worst case", i.e. in which the integration period is maximum, i.e. the exposition lasts 4.42 seconds.

3.5.3 The problem of integration

In order to verify the assumption of constant image speed during the integration period, an additional experiment is performed. An interval of 24 hours was considered with a Δt of 1 ms, and each couple of AC rate spaced the maximum integration period (4420 ms) was considered and the difference of their absolute values was computed. This allows to understand how much the AC rate can vary during the exposition, depending on the value of AC rate itself.

From the analysis, and symply by looking at the picture that represents the evolution of AC rate with time (or simply taking the derivative of ζ'), it is possible to find out that the maximum AC acceleration (the derivative of AC rate) is for the values next to zero. For those values, the AC rate can vary up to 0.217 mas/s during the integration period.

In order to evaluate how much this variation affects the smearing of the image in the AC direction, an interval of 4420 consecutive samples was extracted from the 24-hours sequence in such a way that the AC acceleration within the interval was maximized. In order to do this, the 24-hours sequence was interpolated in order to pass from a resolution of 1 second to a resolution of 1 millisecond.

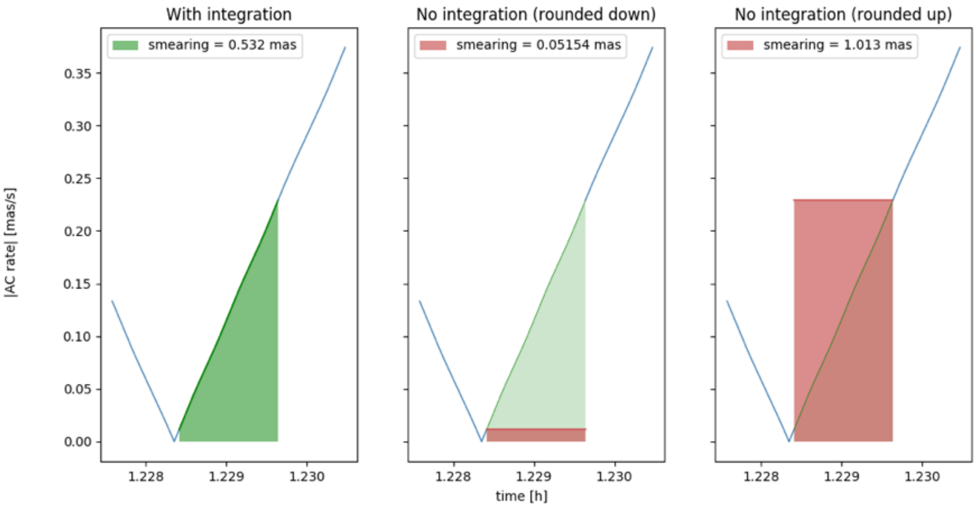

Figure 3.7: Comparison of AC smearing values obtained using integration or approximating a constant AC rate.

From Fig. 3.7 it is possible to observe that in correspondence of values of AC rate near to zero, the AC acceleration is maximum, in the order of 0.217 mas/s during the interval of 4.42 seconds.

Integrating that quantity in the exposition period it is possible to obtain the distance traveled by the image during the integration, and to quantify the consecutive smearing, that results to be in the order of half a milliarcsecond. If, instead of integration, the AC rate is considered constant, the result would be necessarily an approximation of that precise smearing. If, for example, we consider the punctual AC rate at the instant of when the integration starts, we would find, in the same case, a smearing of in the order of 0.05 mas. If we consider for the entire integration the AC rate at the end of the exposition, the smearing would be doubled with respect to the one obtained computing the integration.

Given the results of this analysis and considering the precision required by the *Gaia* specification (in the order of tens of μas), the integration of the along and across rates during the exposition period was preferred for the application of the experiments on real data.

Chapter 4

Experiments and results

The experiments presented below are aimed at quantifying the deformation of the star profiles due to the precession of the satellite, and then at compensating this effect through image scaling. The resulting images are therefore analyzed through image descriptors in order to verify the correct compensation of the periodical effect due to the precession of the satellite and to investigate the presence of other possible periodical variation of the stellar profiles. The software tools implemented and described in Section 3 will be recalled in the following chapters.

Each test is performed iterating in the collection, and executing a pipeline of operations for each observation. This methodology allows to free memory and speed up the process by overwriting the partial results and storing only the final variables at each step of the iteration.

All the presented experiments are performed on one specific CalWrapper provided by OATo, belonging to observations acquired during a nearly-24-hours period starting from 28th January 2018 at 21:37 UTC time. The exposures were detected by the CCD with coordinates (5,4) in the Astrometric Field (AF) and belong to the preceding field of view (FOV1). The stars have magnitude in the gmag bin 9 and have spectral type belonging to the 641.4 nm wavelength bin.

4.1 Preliminary test

As a preliminary operation, an experiment is performed to quantify the smearing effect caused by the vertical speed component of the stars during the transit over the focal plane.

For each exposure of the collection the following procedure is executed:

1. The image is re-scaled in order to allow the subsequent analyses that otherwise would not be possible to perform in a 12x18 pixel^2 area. As mentioned in Sect. 3.3.1, the `OpenCV cv2.resize` method is used, with a scaling factor of 1 to 1000;
2. The algorithm devoted to region of interest (ROI) definition is run, returning the rectangular portion of the image that inscribes the star profile. This operation allows to work on a small portion of the image, reducing the computational cost of the following operations;
3. Image descriptors are computed on the defined ROI, together with two geometrical properties: the ROI area and the ROI aspect. The latter is a fundamental parameter used to quantify the vertical deformation caused by the velocity of the star in the across-scan direction, and is defined as:

$$aspect_{ROI} = \frac{width_{ROI}}{height_{ROI}} \tag{4.1}$$

Once the iteration stops, the set of descriptors computed for each image are collected and evaluated in the time and frequency domain, as indicated in Sect. 3.4.

The results show a predominant periodical component with period of 3 hours, which is totally compliant to the study that is carried out in Sect. 3.5. According to the `AC_rate` value of the `Observation` class computed by AIM software, the stellar profiles appear to be stretched when the star has a consistent trajectory component in the across-scan direction during the transit, as it is possible plotting the evolution in time of the $aspect_{ROI}$ parameter (Fig. 4.1).

Nevertheless, the trend of the $aspect_{ROI}$ values is not smooth, but presents various spikes, which suggests that the deformation of the profiles may depend also on other causes different from the precession of the satellite, or that the ROI detection algorithm described in Sect. 3.3.2 may occasionally converge to a wrong solution.

Also the image descriptors appear to have a strong periodicity in the frequency imprinted by the precession of the spacecraft, which is an indicator of the fact that the image morphology, and not only its geometry, is affected by the blurring effect in the AC direction.

Both the features derived from the histogram of the image and the ones computed starting from the co-occurrence matrix reveal that the vertical deformation of the stellar profiles causes an homogenization of the image

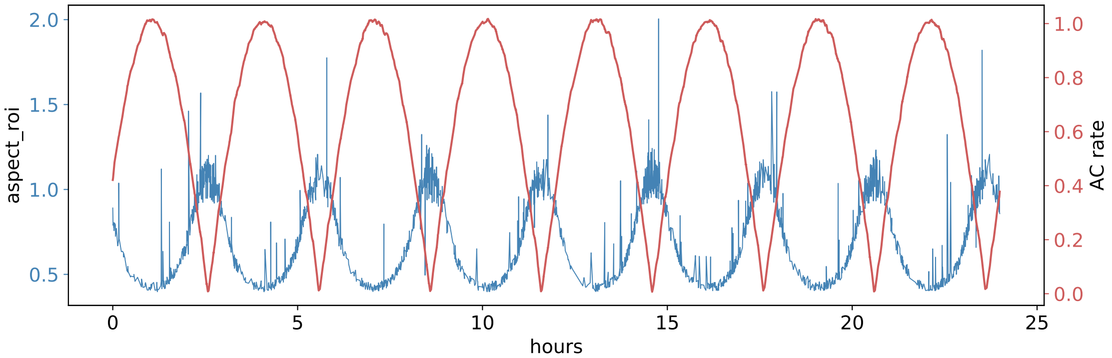

Figure 4.1: The aspect of the region of interests (ROIs) computed for all the images of the collection. The evolution of its value is compliant with the theory and with the empirical `AC_rate` value computed by AIM software (in red).

pattern, with an increase of the *uniformity* and *homogeneity* indicators and a decrease of the *contrast* and *dissimilarity* indexes when the across-scan speed on the focal plane is maximum (Fig. 4.2).

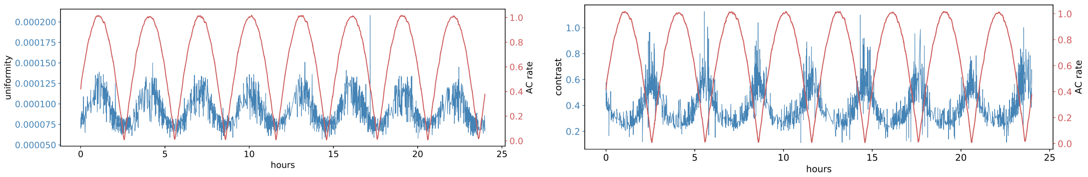

(a) *uniformity* (b) *contrast*

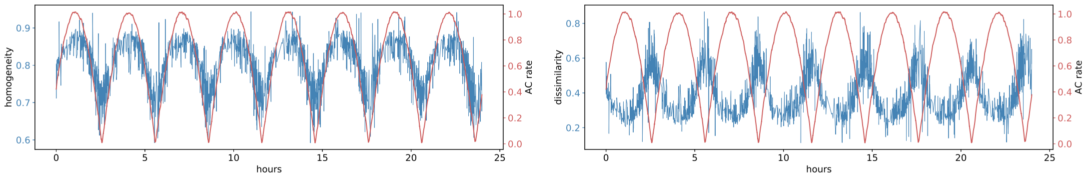

(c) *homogeneity* (d) *dissimilarity*

Figure 4.2: Examples of immage descriptors evaluated in the collection. The *uniformity* index (4.2a) is derived by the evaluation of the image histogram, while contrast (4.2b), homogeneity (4.2c) and dissimilarity (4.2d)indicators are computed within the co-occurrence matrix.

To verify the actual periodical components that appear in the collection, the FFT (Fast Fourier Transform) is executed on the functions described by the image features in the 24-hours period. The analysis confirms the presence of a predominant component with period of 3 hours for any of the computed descriptors. Except from a secondary peak relative to the period of 90 minutes (1.5 hours), probably related to an harmonic of the main frequency, the other frequency components result to be negligible (Fig. 4.3).

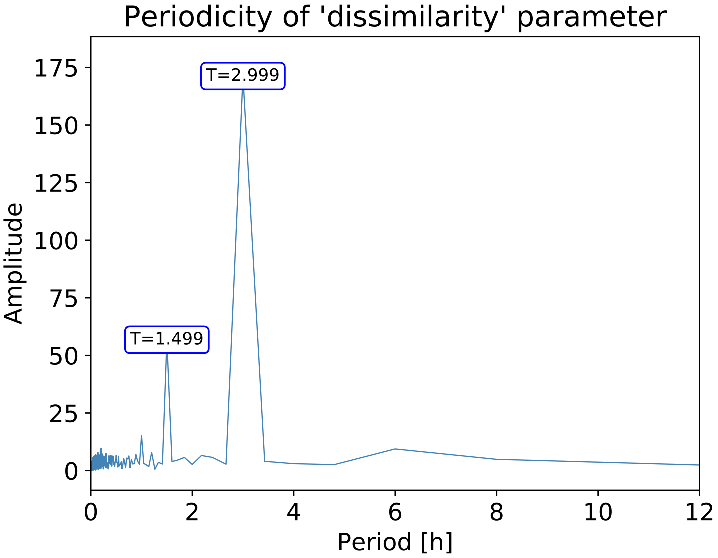

Figure 4.3: Fast Fourier Transform computed for one of the image descriptors (*dissimilarity*). The frequency relative to the period of 3 hours has the highest peak. A secondary peak at $T = 1.5$ hours appear.

4.2 Experiment I (profile shrinking using ROI aspect)

4.2.1 Implementation

As mentioned in Section 4.1, the ratio between the width and the height of the region of interest that inscribes the star profiles can be used as an index to quantify the deformation of the stellar images.

The straightforward idea that underpins the following experiment is to use again the ROI's aspect to define an asymmetrical transformation to compensate the inverse deformation that caused the smearing of the image. Supposing that the stretch is only in the vertical direction, it is possible to hypothesize that shrinking the image in the opposite direction in a proper way would allow to easily deconvolve the blurring effect.

In this direction, the procedure iterates on the images of the collection and performing at each step the following operations:

1. Image scaling by a x1000 factor: a new 1200x1800 is obtained, allowing a finer definition of the region of interest.
2. The algorithm devoted to ROI definition is run, returning the portion of the image that inscribes the star profile.
3. The aspect of the ROI is computed, following Eq. 4.1.
4. ROI's aspect is used to determine a new scaling factor, in order to shrink the star profiles and compensate the deformation due to precession. In particular, supposing a deformation only in the vertical direction, it is possible to compensate it by rescaling the original image changing its proportions: instead of creating a new $x_{dim} * y_{dim}$ image, the original window is scaled into a $x_{dim} * (y_{dim} * aspect_{ROI})$ image.
5. The ROI is again computed in order to verify that the profile is actually shrunk and to allow the analysis of the image descriptors.
6. Image descriptors are evaluated.

Then, the resulting features of all the observations are analyzed in the time and frequency domain, to verify the effective compensation of the smearing and to search for other periodical variations in the star profiles.

4.2.2 Results

The results of the image shrinking are inferred from the time domain and frequency domain plots.

Computing the ROI's aspect after the profile shrinking operation it is possible to verify that the star profiles have been correctly scaled down: all the exposures now present nearly-circular blobs ($aspect_{ROI} \approx 1$). Not all the images are perfectly shrunk ($aspect_{ROI} = 1$) as the ROI's aspect oscillates between 0.995 and 1.005, probably due to decimal rounding (Fig. 4.4).

Nevertheless, the image descriptors reveal that, despite having geometrically removed the effect of the smearing, the image properties derived from pixel intensity are still affected by the deformation that the image undergoes during the exposure (Fig. 4.5).

Still, the FFT confirms that the 3-hours periodicity is the predominant component in the frequency domain (Fig. 4.6).

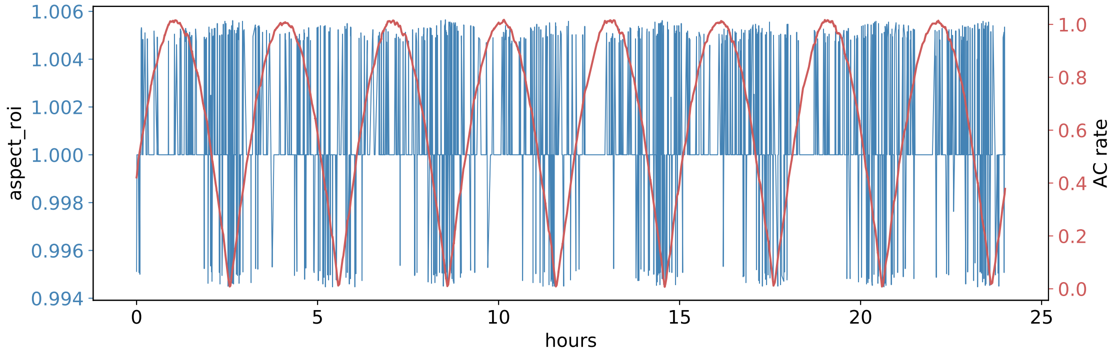

Figure 4.4: $aspect_{ROI}$ parameter, evaluated for the entire collection after the image scaling.

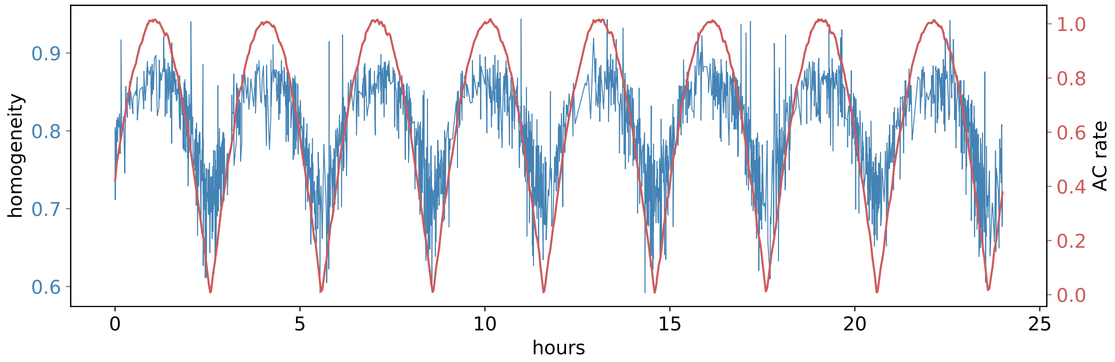

(a) *homogeneity*

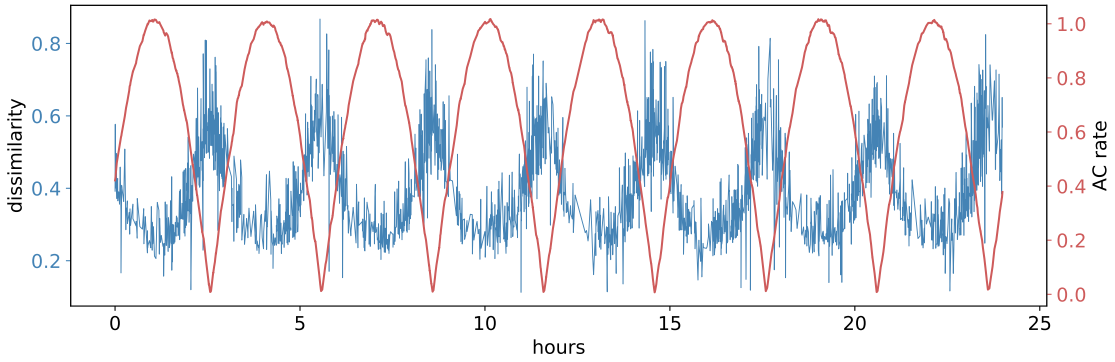

(b) *dissimilarity*

Figure 4.5: Image descriptors evaluated after the image shrinking using the asymmetric image scaling.

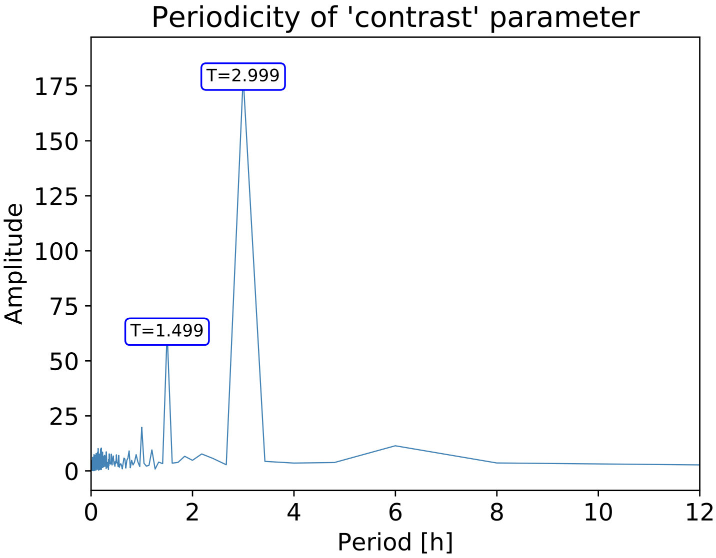

Figure 4.6: Periodical *components* of the correlation parameter after the image shrinking .

4.3 Experiment II (profile shrinking using PCA)

4.3.1 Implementation

The following procedure proposes an alternative approach for profile shrinking. In detail, instead of computing the ROI aspect and using image scaling to compensate the deformation, the proposed method makes use of *Principal Component Analysis* (PCA).

PCA is a linear transformation commonly used in statistics that transforms the data into a new set of coordinates, called *principal components*, such that the first component has the largest possible variance, and each succeeding component in turn has the highest variance possible. It results in a new orthogonal basis set.

In this case, the solution consists in finding a new pair of axes that better fit the points that represent the star profile, resulting in a rotation of the profile itself.

Given an image with intensities $I(x, y)$, we can compute its raw moments M_{ij} as:

$$M_{ij} = \sum_x \sum_y x^i y^j I(x, y) \tag{4.2}$$

Once obtained the raw moments, we can define the central moments μ_{pq}

with respect to the centroids defined by the two components: $\overline{x} = \frac{M_{10}}{M_{00}}$ and $\overline{y} = \frac{M_{01}}{M_{00}}$.

$$\mu_{pq} = \sum_x \sum_y (x - \overline{x})^p (y - \overline{y})^q f(x, y) \tag{4.3}$$

Then, central moments allow to calculate the covariance matrix of the image, fundamental for the execution of the principal component analysis:

$$cov[I(x, y)] = \begin{bmatrix} \mu'_{20} & \mu'_{11} \\ \mu'_{11} & \mu'_{02} \end{bmatrix} \tag{4.4}$$

For the scope of computing the image moments, the `OpenCV` class `cv2.moments` is used.

An alternative approach for defining the covariance matrix has been also implemented executing a curve fitting of the star profile with a bivariate Gaussian distribution, but it resulted to be inefficient in terms of execution time.

Then, eigenvalues $L = [\lambda_0, \lambda_1]$and eigenvectors $U = \begin{bmatrix} u_{00} & u_{01} \\ u_{10} & u_{11} \end{bmatrix}$ of the covariance matrix can be computed. In this case `linalg.eigh` method of `NumPy` library is used.

A new set of coordinates can therefore be computed rewriting the original ones with respect to the new reference system defined by the eigenvectors U:

$$z_1 = u_{00}(X - \overline{x}) + u_{01} * (Y - \overline{y}) \tag{4.5}$$

$$z_2 = u_{10}(X - \overline{x}) + u_{11} * (Y - \overline{y}) \tag{4.6}$$

where X and Y are the original set of indexes of the image points. The new set of coordinates result to be rotated and centered in the new reference system.

In order to shrink and normalize the star profile, each coordinate can be divided by the standard deviation on the respective direction, defined by$\sqrt{\lambda_0}$ and$\sqrt{\lambda_1}$:

$$w_1 = \frac{z_1}{\sqrt{\lambda_0}} + \overline{x} \tag{4.7}$$

$$w_2 = \frac{z_2}{\sqrt{\lambda_1}} + \overline{y} \tag{4.8}$$

where the offsets $\overline{x}$ and $\overline{y}$ are used to suit the pixel coordinates, where the origin 0,0 is located in the upper-left of the image. Then, a *bicubic* interpolation is used to re-sample the image, in order than it is regularly sampled.

Once the profiles are reshaped, a region of interest is defined within the images in order to perform the analyses on the histogram and on the co-occurrence matrix.

4.3.2 Results

The results obtained by applying PCA to the re-scaled images do not satisfy the precision required by the mission specification. PCA only partially manages to shrink the stellar profiles and a residual deformation remains, especially for high levels of across-scan motion (Fig. 4.7).

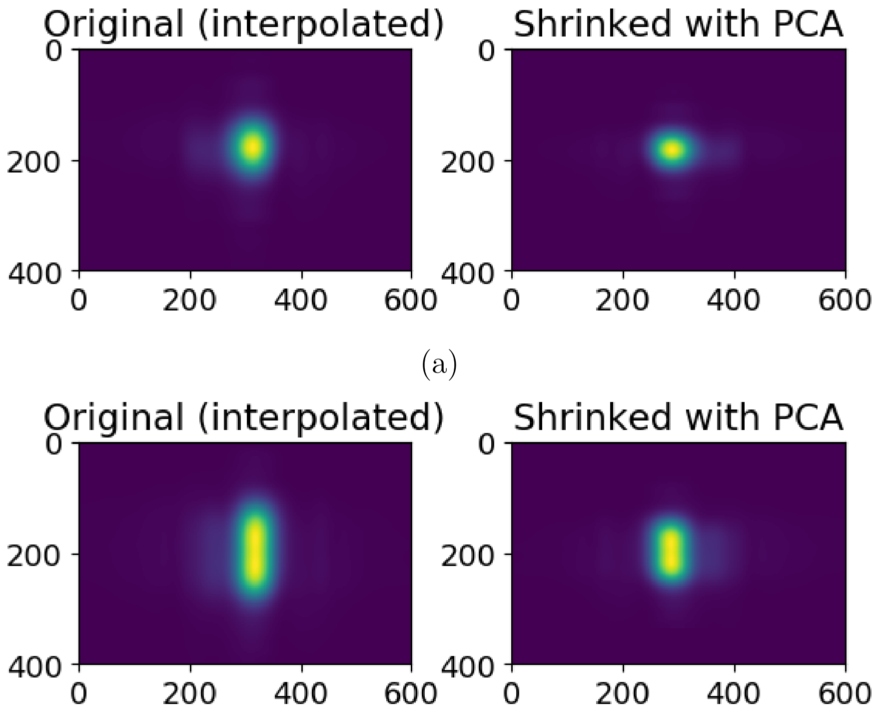

(a)

(b)

Figure 4.7: Result of image shrinking using PCA transformation. For high levels of AC motion (4.7b) the deformation is not totally compensated.

As a consequence, also the image descriptors show a strong periodical component of 3 hours, that is highlighted both in the time-domain and the frequency-domain representation.

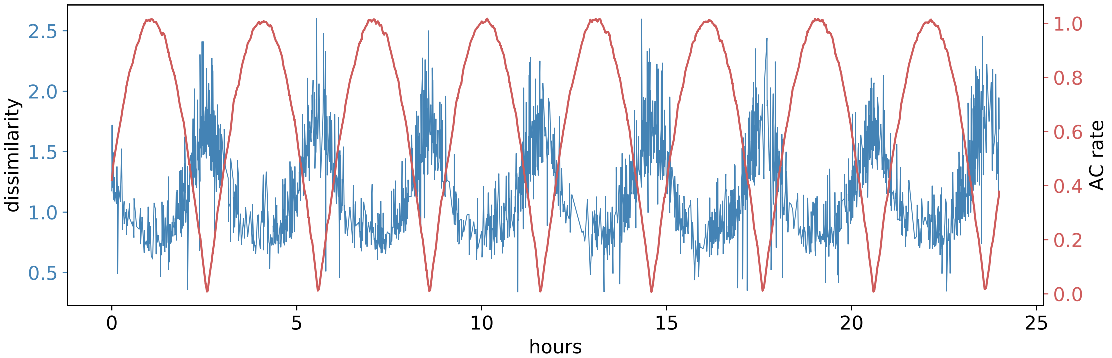

(a)

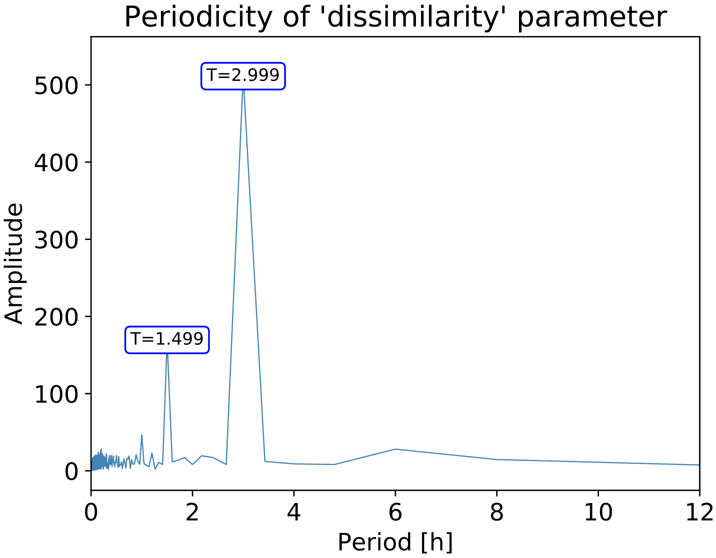

(b)

Figure 4.8: *Dissimilarity* descriptor evaluated after the PCA transformation in time (4.8a) and frequency domain (4.8b).

4.4 Experiment III (profile shrinking using NSL model)

4.4.1 Implementation

The following experiment is aimed at compensating the AC (and AL) motion blurring effect making use of the attitude model presented in section 3.5.1. This allows to shrink the stellar profiles according to the exact evaluation of the deformation, avoiding to introduce errors that depend on the method that is used for defining the amount of smearing, such as the ROI evaluation.

In order to evaluate the instantaneous speed of the images among the focal plane it is necessary to make use of the Fortran routine provided by SOFA. The computation of the across-scan and along-scan rates requires nevertheless the knowledge of the parameters Ω_0 and ν_0, respectively the *initial heliotropic spin phase* and the *initial precession angle*, that are not known a priori. Since the two parameters are defined as $\Omega_0 = \nu_0 = 0$ for epoch J2000.0, it is possible to use the SOFA algorithm itself to determine their values for each exposure [12].

The routine, as previously mentioned, takes as input the initial date, the final date, and the sampling interval for which we want to compute the attitude parameters. In this case, the algorithm is run the first time setting the initial date to the J2000.0 epoch, and the final date according to the timestamp of the observation we want to analyze, i.e. the instant in which the exposure started. Since we are just interested in the values of Ω and ν at the timestamp value, it is possible to set the sampling interval as the entire time period from J2000.0 to the timestamp in order to get only one entry. Once Ω_0 and ν_0 are retrieved for the initial time instant of the integration, it is possible to use them to set the Fortran routine for the calculation of the across and along rates (ζ' and η') values during the exposure.

Thus, for each image of the collection, the following procedure can be defined:

1. Retrieve Ω_0 and ν_0 relative to the first instant of the integration using the Fortran routine;

2. Call again the routine to get the instantaneous velocities ζ' and η'during the integration period. The duration of the exposure is inferred by the attribute `Observation.integration_time`;

3. Integrate the rate values according to the exposure period in order to obtain the shift of the image both in across and along directions, expressed in milliseconds of arc;

4. To define the actual shape of the blurred profiles it is necessary to add the angular shift to the original angular dimensions of the diffraction profile produced by the rectangular aperture of the telescope. It is possible to have an approximate estimation of the dimension of star profiles using

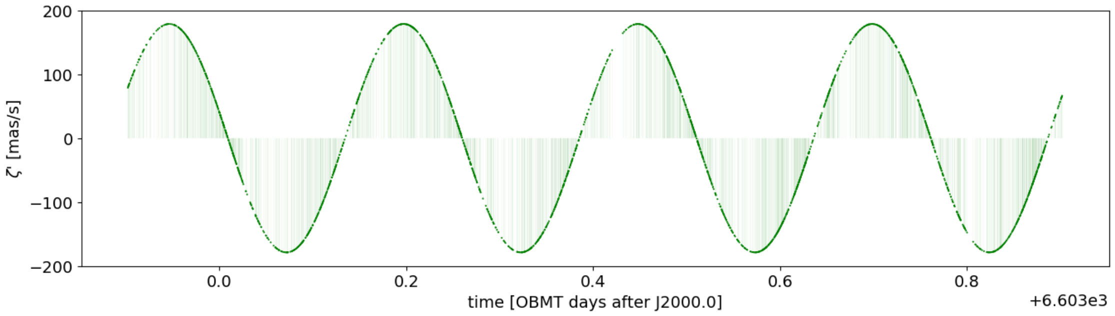

Figure 4.9: The figure shows in green the values of ζ' that relative to the integration period of the exposures that compose the wrapper.

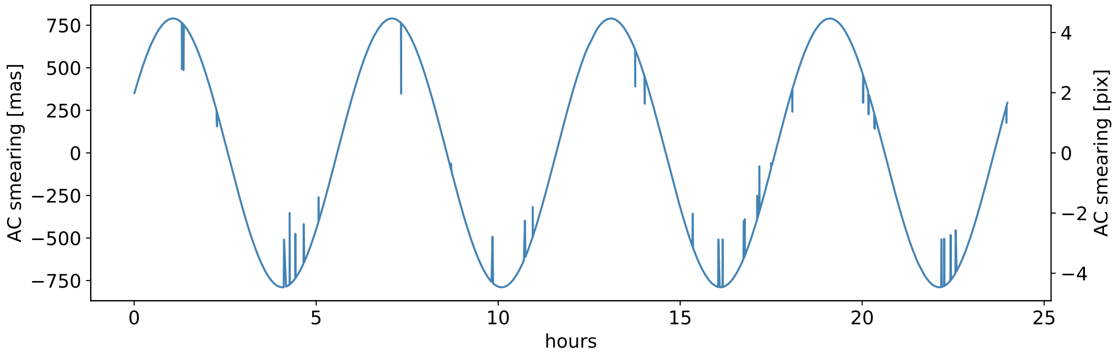

Figure 4.10: Smearing in the across-scan direction, evaluated for the whole collection of observations, both in milliseconds of arc and in pixels. The spikes are due to the application of a different gating, resulting to a reduced integration time.

the following formulas:

$$d_{AL} = \frac{2\lambda F}{D_x}, d_{AC} = \frac{2\lambda F}{D_y} \tag{4.9}$$

where λ is the main wavelength of the source, F is the focal length of the telescope and D_x , D_y are the dimensions of the rectangular aperture (Fig. 4.11). The obtained quantities have to be converted into angular dimensions in order to match with the calculation of the smearing.

5. In order to the smearing effect and obtain the original shape of the stellar profile, the angular shift has to be converted into pixels in such a way that it describes the deformation impressed on the focal plane. The

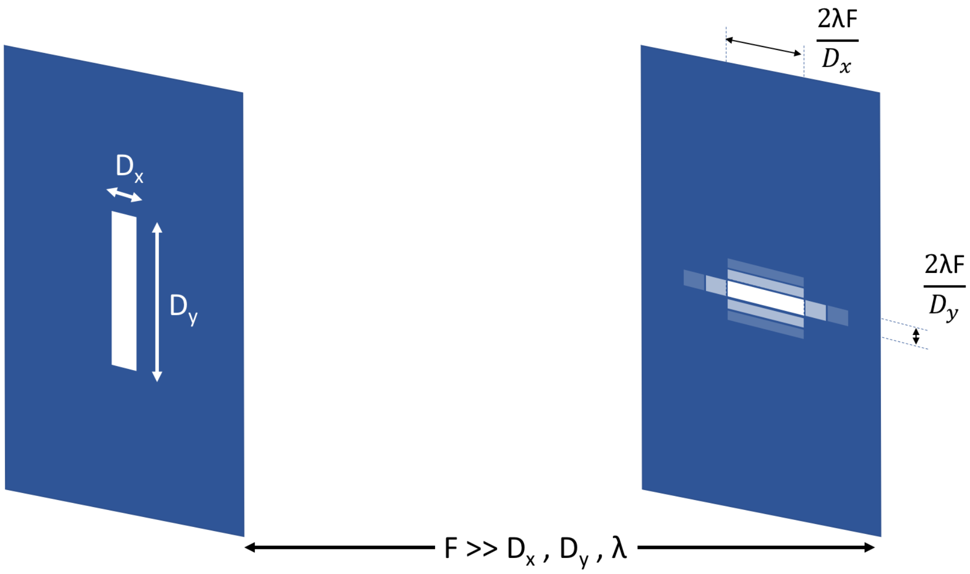

Figure 4.11: Graphical representation of the diffraction profile produced by a rectangular aperture.

relations used to apply this conversion are the following:

$$smearing^{px}_{AC} = (smearing^{arc}_{AC} + d_{AC})/px^{arc}_{AC} \tag{4.10}$$

$$smearing^{px}_{AL} = (smearing^{arc}_{AL} + d_{AL})/px^{arc}_{AL} \tag{4.11}$$

where px^{arc}_{AC} and px^{arc}_{AL} are the pixel angular dimensions, respectively in the across and along direction, and d_{AC}, d_{AL} are the approximate dimensions of the PSF computed at step 4. ;

6. The blurring effect can be compensated by computing the ratio between the smearing in along and across direction, and then by applying the same transformation performed in Sect. 4.2;

7. A region of interest is defined within the image and the image descriptors are evaluated.

4.4.2 Results

The values of the across-scan velocities obtained by applying the NSL model turn out to be shifted in time with respect to the sperimental values of *AC rate* computed by the DPAC software.

In detail, comparing the evolution in time of the two functions within the 24-hours period of the collection, the theoretical instantaneous speeds appear to be about 25 minutes (plus n periods) ahead in time with respect to the empirical values of *AC rate* (See Fig. 4.12a).

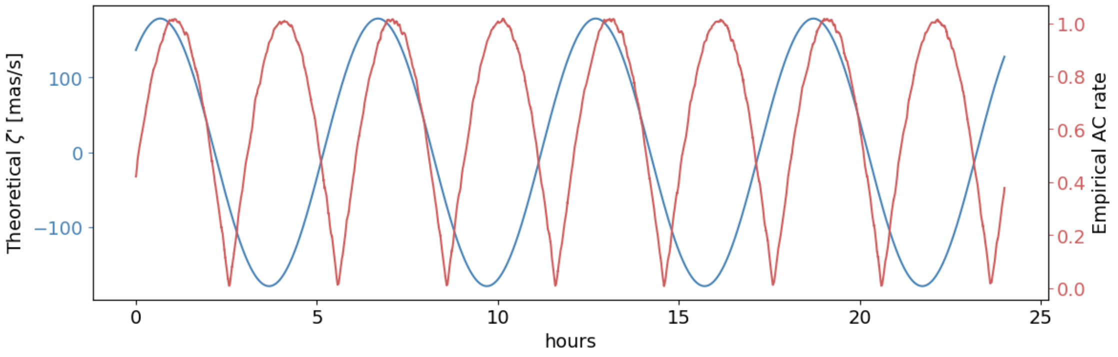

(a) Before safe mode

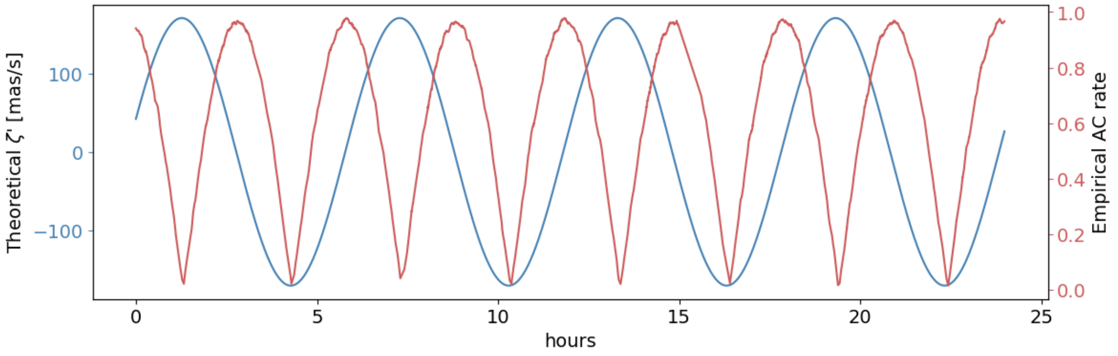

(b) After safe mode

Figure 4.12: Comparison of the theoretical and empirical evaluation of *AC rate*. 4.12a refers to the wrapper dated 28th January 2018 (134184247825612800 OBMT); 4.12b refers to the wrapper dated 30th April 2018 (142133050132480000 OBMT).

The most credited hypotheses about the causes of this unexpected behaviour were either an error in setting the initial parameters Ω_0 and ν_0, or the occurrence of safe modes in the *Gaia* payload, which may have caused a divergence between the expected attitude and the actual spacecraft orientation.

In order to verify the last hypothesis, a new calibration wrapper is considered. The wrapper was acquired on 30th April 2018, which is following a safe mode that occurred on 18th February 2018. Safe modes are triggered when the spacecraft parameters exceed their thresholds and the spacecraft automatically takes measures to preserve its safety. During the safe modes, science instruments are disabled in order to protect them, and the communication with Earth is performed using the spacecraft's low-gain antenna [13].

As the wrapper originally considered in this work is dated 28th January 2018 (that is prior to the safe mode occurrence), it is possible to compare the evolution in time of the across-scan rates in both the configurations and verify if the time shift with respect the experimental values has changed.

The result, represented in Fig. 4.12b, show that the time shift between the expected velocities and the empiric measurements has changed after the *Gaia* payload has entered the safe mode.

Thus, it is possible to validate the hypothesis that a reset of the *Gaia* onboard system may have introduced a variation in the expected configuration, which was not modeled by the SOFA Fortran routine.

The exact shift between the two wave functions is computed by performing the cross-correlation of the two sequencies. A preliminar step consists in taking the absolute values of the velocities computed by the Fortran software and scaling them in the interval between 0 and 1. This transformation makes the two sequencies more similar and allows a more accurate estimation of the shift. The correlation between the two periodic digital sequencies is then computed applying the following relation:

$$xcorr(x,y) = IFFT(FFT(x)FFT(y)^*) \tag{4.12}$$

and finding the corresponding time coordinate of the maximum peak.

The resulting values of time shift are 23.901 minutes (plus n periods) for the collection prior to the safe mode, and 92.722 minutes (plus n periods) for the wrapper collected after the safe mode. Those values are used to properly re-align the NSL mathematical model with the measured AC rates in order to correctly compensate the deformation of the star profiles.

The results of the image shrinking show that the described methodology succeeds in mitigating the deformation due to the AC motion, but fails in totally compensating it. In detail, images affected by high across-scan rates are not enough restored, as they present an aspect ratio of 0.8/0.9 after the shrinkage; images with low values of AC rate appear, instead, to have suffered an excessive flattening so that the aspect ratio is in the order of 1.2/1.3 (Fig. 4.13).

Like the shape of the stellar profiles, also their morphological properties are not totally compensated by the shrinking procedure. Each descriptor still

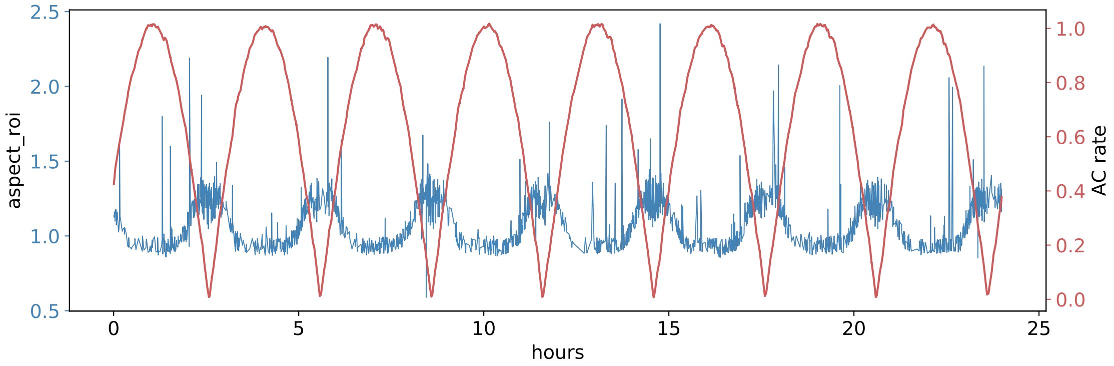

Figure 4.13: $aspect_{ROI}$ evaluated after shrinking the images using the scanning law model.

presents a predominant periodical component of 3 hours, so it is possible to state that the current methodology does not allow to eliminate the effect of the AC motion and to remove that variable from the calibration procedure (Fig. 4.14).

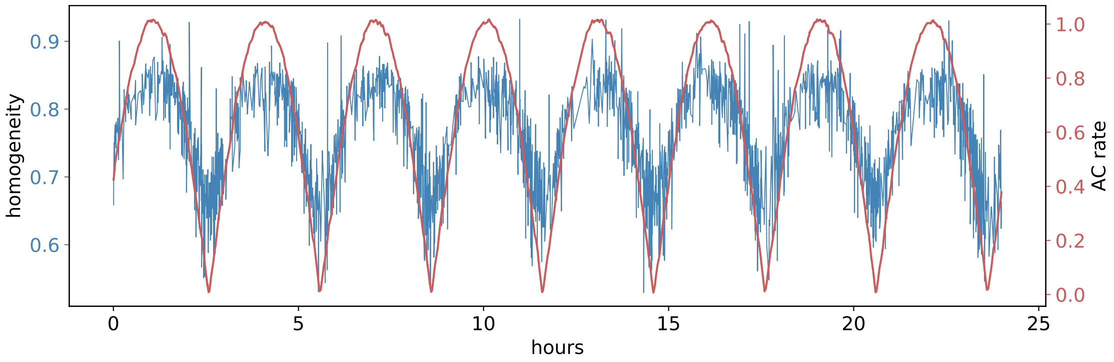

Figure 4.14: *Homogeneity* descriptor evaluated for the entire collection.

Chapter 5

Conclusion and possible developments

The thesis work was focused in implementing an alternative approach for *Gaia* astrometric data calibration. The aim was to have an independent evaluation of the PSF star profiles for each observation, in order to minimize the variables and the errors introduced in the procedure. In particular, the effort has been put on the compensation of the AC (and AL) motion effect.

The performed methodologies, which consisted in the application of image re-scaling algorithms, allowed only to mitigate and not to completely eliminate the deformation of the stellar profiles produced by the precession of the spacecraft. In addition, the evaluation of image descriptor allowed to better quantify the effectiveness of the deconvolution algorithms applied to the observations: in any case it showed that even well-shaped profiles still suffer, in terms of pixel-by-pixel properties, the deformation caused by the AC motion. It could mean that the blur caused by the motion of the star on the focal plane impact irreversibly on the quality, and not only the shape, of the astrometric images.

In particular, Experiment III (Sect. 4.4), was thought as a methodology that could quantify the exact smearing in a way totally independent from the other variables that are involved in the image acquisition. Nevertheless, few approximations could not be avoided during the procedure, impacting on the exactness of the procedure. The occurrence of safe-modes and the consequent deviation of the scanning law model from its nominal behaviour, for example, introduced a perturbation in the processing that could have been not totally repaired by the re-alignment using correlation. For this purpose, other parameters could be considered in order to exactly know where the spacecraft is pointing in a specific time instant.

An other possible improvement in the procedure could be the development of an ad-hoc interpolation algorithm to shrink the stellar images, in order to minimize the amount of spurious information introduced in the processing.

The procedure of compensating the stellar motion will become then totally independent from any external after studying a proper methodology to shrink the profiles ignoring the knowledge of the PSF dimensions, which are not exactly known a priori.

Finally, the proposed methodology could be compared to the traditional processing routine only after applying PSF modeling to the single exposures cleaned by the AC motion deformation.

Nomenclature

AC Across-Scan direction

AIM Astrometric Instrument Model

AL Along-Scan direction

BAM Basic Angle Monitor

CCD Charge-Coupled Device

DPAC Data Processing and Analysis Consorsium

DPCT Data Processing Center of Turin

ESA European Space Agency

FFT Fast Fourier Transform

FOV Field Of View

FWHM Full Width at Half Maximum

INAF Istituto Nazionale di AstroFisica

LSF Line Spread Function

OATo Osservatorio Astrofisico di Torino

PCA Principal Component Analysis

PSF Point Spread Function

ROI Region Of Interest

TDI Time Delayed Integration

Bibliography

[1] Michael Perryman (2012) *"The history of astrometry"*, The European Physical Journal H, Volume 37, Issue 5, pp 745-792

[2] T. Prusti et al. (2016) *"The Gaia mission"*, Astronomy & Astrophysics, Volume 595 , A1

[3] Deborah Busonero et al. (2014) *"Running AIM: initial data treatment and mu-arcsec level calibration procedures for Gaia within the Astrometric Verification Unit"*, Proceedings of SPIE - The International Society for Optical Engineering, 9150:91500K

[4] Deborah Busonero et al. (2014) "*Astrometric Instrument Model software tool for Gaia real-time instrument health monitoring and diagnostic*"

[5] Mario Gai, Deborah Busonero (2013) *"Statistically Optimal Fitting of Astrometric Signals"*, PASP, 125, pp 444-455

[6] Lennart Lindegren (2012) *"The astrometric core solution for the Gaia mission"*

[7] Claus Fabricius et al. (2016) *"Gaia Data Release 1 - Pre-processing and source list creation"*, Astronomy & Astrophysics, 595, A3

[8] ESA, DPAC (2018) *"Gaia Data Release 2"*, v1.1, (https://gea.esac.esa.int/archive/documentation/GDR2)

[9] Rafael C. Gonzalez, Richard E. Woods (2007) "*Digital Image Processing"*, 3rd edition, Prentice Hall, pp 828-836

[10] Mryka Hall-Beyer (2017) *"GLCM Texture: A Tutorial"*, v. 3.0

[11] Lennart Lindegren (2004) *"The speed of a star image in the Gaia field of view from a general attitude motion or scanning law"*, GAIA–LL–056

[12] Lennart Lindegren (2001) *"Calculating the GAIA nominal scanning law"*, SAG-LL-35

[13] 21st March 2018, "Gaia status update: safe mode and recovery", http://sci.esa.int/jump.cfm?oid=60098